1 **CDK1 and CDK2 regulate phosphorylation-dependent NICD1 turnover**

2 **and the periodicity of the segmentation clock**

3

4

5 **Francesca Anna Carrieri[1], Philip Murray[2], Paul Davies[3], Jacqueline Kim Dale[1*]**

6

7 [1]Division of Cell and Developmental Biology, School of Life Sciences, University of Dundee,

8 Dow Street, Dundee, DD15EH, Scotland, UK.

9 [2]Department of Mathematics, University of Dundee, Nethergate, Dundee, DD14HN, Scotland,

10 UK.

11 [3]MRC Phosphorylation Unit, School of Life Sciences, University of Dundee, Dow Street,

12 Dundee, DD15EH, Scotland, UK.

13

14

15 * Corresponding author: j.k.dale@dundee.ac.uk

16 Tel: +44 01382 386290

17   **ABSTRACT**

18   All vertebrates share a segmented body axis. Segments form periodically from the rostral end

19   of the presomitic mesoderm (PSM) and this periodicity is regulated by the segmentation clock,

20   a molecular oscillator that drives dynamic clock gene expression across the PSM with a

21   periodicity that matches somite formation. Notch signalling is crucial to this process. Altering

22   Notch intracellular domain (NICD) stability affects both the clock period and somite size.

23   However, the mechanistic details of how NICD stability is regulated are unclear.

24   We identified a highly conserved site crucial for NICD recognition by the SCF E3 ligase, which

25   targets NICD for degradation. We demonstrate both CDK1 and CDK2 can phosphorylate

26   NICD in the domain where this crucial residue lies and that NICD levels vary in a cell cycle-

27   dependent manner. Inhibiting CDK1 or CDK2 activity increases NICD levels both *in vitro* and

28   *in vivo*, leading to a delay of clock gene oscillations.

29 **INTRODUCTION**

30   Segmentation, a process which occurs early during vertebrate body plan formation, generates

31   repeated segments (or somites) that later give rise to the vertebral column, most skeletal

32   musculature and dermis [1, 2].

33   During somitogenesis, pairs of somites bud off the rostral end of the unsegmented presomitic

34   mesoderm (PSM) with a periodicity that is species specific. The periodicity of segment

35   formation is regulated by a molecular oscillator, known as the somitogenesis clock, which

36   drives oscillatory gene expression within the PSM tissue from which somites are derived [2-

37   4].

38   These clock genes are targets of the Notch, Wnt and FGF pathways [5, 6]. Aberrant

39   somitogenesis leads to severe segmentation and skeletal defects [7]. In humans, defects in

40   segmentation lead to congenital scoliosis (CS), with an infant mortality rate of 50% that

41   comprises many vertebral skeletal and muscular pathologies, including the family of

42   spondylocostal dysostoses (SCD). For CS, whilst the aetiology is unclear, linkage analyses

43   have shown mutations in four genes lead to familial forms of SCD [8]. Significantly these are

44   components of the Notch pathway, which plays multiple roles during segmentation. Notch is

45   crucial to the segmentation process in mice, since in the absence of Notch signalling, the

46   segmentation clock stops and no somites form [9].

47   On a single cell level in the PSM, oscillatory clock gene expression is established through

48   positive and negative feedback loops of unstable clock gene products which potentiate or

49   inhibit the pathway that activates them. Synchronisation of clock gene oscillations between

50   neighbouring cells is reliant on Notch signalling [10-13]. Mathematical models predict the

51   period of clock gene oscillations can be approximated as a sum of the delays involved in

52   transcription, splicing, translation and transport of clock gene products, and in particular

53   through the regulation of the half-lives of both mRNA and protein of unstable regulators [14-

54   17]. Whilst great progress has been made in demonstrating the role of transcription and

55   splicing delays in setting the clock period, little experimental work investigating whether

56   stability of clock components affects clock period has been performed.

3

57 Most studies addressing the molecular mechanisms regulating the periodicity of clock gene

58 oscillations have focused on the role of Notch signalling components [10, 18-23]

59 Notch is one of the major highly conserved signalling pathways that regulate cell-cell

60 communication which involves gene regulation mechanisms that control multiple processes

61 during development and adult life [24-31].

62 Upon extracellular ligand activation, Notch transmembrane receptors are cleaved, releasing

63 the intracellular domain (NICD) that translocates to the nucleus to regulate expression of

64 specific developmental gene cohorts [30, 32, 33]. NICD is highly labile, and phosphorylation-

65 dependent turnover acts to restrict Notch signalling [34-36].

66 All known canonical Notch activity relies on this regulation of NICD half-life. Moreover,

67 aberrant NICD turnover contributes to numerous cancers and diseases [24, 28, 37-42].

68 Despite the multiple impacts of NICD turnover in both development and disease, the molecular

69 details regulating this turnover remain uncharacterised. The stability of NICD and therefore

70 duration of the Notch signal is regulated by phosphorylation of the C-Terminal PEST domain

71 which leads to subsequent recruitment of FBXW7, F-Box and WD Repeat Domain Containing

72 7, (a key component of the $SCF^{Sel10/FBXW7}$ E3 ubiquitin ligase complex) [34-36, 43-49].

73 Ultimately, this leads NICD to ubiquitylation and proteasomal degradation [43, 50-53].

74 However, the molecular details of NICD degradation mediated by FBXW7 are not well

75 understood.

76 A recent study combining experimental and computational biology demonstrated changes in

77 NICD stability affect the chick and mouse somitogenesis clock period which in turn affects

78 somite size. In this study a pharmacological approach was used to demonstrate that culturing

79 chick/mouse PSM explants with broad specificity inhibitors of cyclin-dependent protein

80 kinases (Roscovitine/DRB) and Wnt signalling (XAV939) leads to elevated levels and a

81 prolonged NICD half-life and phase shifted clock oscillation patterns both at a tissue level and

82 in larger segments. Furthermore, reducing NICD production in this assay rescues these effects

83 [18]. These results imply potential coupling between NICD degradation and the segmentation

84   clock. However, the specific kinases/molecular mechanism of action remain ill-defined and

85   leave open the question of whether this coupling is a general or conserved mechanism.

86   In this manuscript we identify the phosphorylated residues within human NICD. We

87   demonstrate that purified recombinant Cyclin-dependent kinase 1 (CDK1) and Cyclin-

88   dependent kinase 2 (CDK2) phosphorylate NICD within the PEST domain. A point mutation

89   affecting a conserved serine residue within this CDK substrate domain of the NICD PEST

90   motif prevents NICD interaction with endogenous FBXW7. Strikingly, we show that NICD

91   levels fluctuate in a cell cycle dependent manner anti-correlating with high levels of CDK1/2

92   activity. Lastly, highly specific inhibitors of CDK1 or CDK2 lead to increased levels of NICD *in*

93   *vitro* and *in viv*o and delay the mouse somitogenesis clock and somite formation.

94   Using a mathematical model we show that the experimental observations made in cell lines

95   and PSM tissue can be explained in a single theoretical framework that couples the cell cycle

96   to NICD degradation.

RESULTS

Roscovitine, DRB and XAV939 increase NICD levels in HEK293, iPS and IMR90 cells

Direct phosphorylation of NICD in its PEST domain enhances its turnover and thus degradation [34-36]. A study using broad range kinase inhibitors demonstrated that the stability and turnover of NICD is linked to the regulation of the pace of the segmentation clock across the PSM in chick and mice embryos [18]. However, this study did not define the specific kinases or molecular mechanism of action of the inhibitors. In order to identify which kinases are involved in NICD phosphorylation and which residues in the NICD PEST domain are phosphorylated rendering NICD susceptible to degradation, we employed a cellular model due to the limiting quantity of material available using embryonic cell lysates.

First, we used the same inhibitors as Wiedermann *et al.* [18], and thus investigated if Roscovitine, DRB and XAV939 elicit the same effect upon NICD levels in a variety of cell culture models, namely HEK293 (human embryonic kidney), iPS (induced pluripotent stem cells) and IMR90 (human Caucasian foetal lung fibroblast) cells.

Roscovitine is a small molecule belonging to the family of purines. It inhibits cyclin-dependent kinases (CDKs) through direct competition with ATP for binding at the ATP-binding site of CDKs [54, 55]. DRB (5,6-dichloro-1-β-D-ribofuranosylbenzimidazole) also inhibits CDKs, particularly CDK7 and 9 [56, 57]. XAV939 is a Wnt inhibitor that stimulates β-catenin degradation by stabilizing axin through inhibition of the enzymes tankyrase 1 and 2 [58].

HEK293, iPS or IMR90 cells treated for 3 hours with each of the three inhibitors at the same concentrations used in embryonic lysate studies [18] led to an increase in NICD levels compared to control cells cultured in the presence of DMSO (**Figures 1A-D, Supplementary Figure 1**). In control conditions, NICD was not easily detectable due to its very short half-life. Quantification of the density of western blot bands in at least three independent experiments confirmed that the increase in NICD levels was statistically significant after treatment with Roscovitine, DRB and XAV939, as shown in **Figures 1B, 1D and Supplementary Figure 1B**. Two other inhibitors were used as positive and negative controls for the assay. LY411575 is a γ-secretase inhibitor that prevents Notch1 cleavage and thus inhibits activation of target

6

125 gene expression [59, 60]. As expected, LY411575 treatment significantly reduced NICD levels

126 (**Figures 1A-D, Supplementary Figure 1**). Phosphorylation of the C-Terminal PEST domain

127 of NICD leads to recruitment of FBXW7 and thus to NICD ubiquitylation and proteasomal

128 degradation [34-36, 43, 44, 46-48]. When E3 ligase activity is reduced with the NEDDylation

129 inhibitor MLN4924 [61], NICD levels increase, since NICD degradation is stopped in the

130 presence of this compound (**Figures 1A-D, Supplementary Figure 1**).

131 Interestingly, we were able to detect two distinct bands by western blot with the NICD antibody,

132 particularly when cells were treated with MLN4924. We hypothesised this reflected the

133 presence of non-phospho and phospho-NICD species. To test this hypothesis, we treated

134 MLN4924-treated lysates with λ phosphatase which abrogated the appearance of the higher

135 band by western blot with the NICD antibody (**Figures 1A and 1C**). These data demonstrate

136 that the higher band detected corresponds to a phosphorylated isoform of NICD.

137 In order to determine if the increased levels of NICD were due to increased NICD production

138 and/or increased NICD stability, we exposed HEK293 cells to LY411575 treatment for the last

139 hour of culture, thereby inhibiting the production of new NICD. Under control conditions with

140 LY411575 treatment in the last hour, NICD levels are very low (**Supplementary Figure 2,**

141 **lane 2**). However, despite LY411575 treatment in the last hour, cells cultured in the presence

142 of small molecule inhibitors showed increased levels of NICD compared to the control,

143 indicating that the increase in NICD levels is not due to increased NICD production, but to an

144 increased stability (**Supplementary Figure 2**).

145 Taken together, these results show that exposure to this group of inhibitors leads to increased

146 levels of NICD in a variety of cell lines, in the same way that they do in the mouse and chicken

147 PSM tissue, suggesting they regulate a conserved mechanism leading to increased NICD

148 levels and reduced NICD turnover.

149

150 **Phostag analysis following Roscovitine, DRB and XAV939 treatment reveals a variety**

151 **of NICD phospho-species.**

152   In order to investigate whether this selection of small molecule inhibitors have different effects

153   on NICD phosphorylation, we treated HEK293 cells with the inhibitors and performed a Phos-

154   tag assay [62]. Following MLN4924 treatment, a variety of bands indicative of different

155   phospho-species of NICD was observed (**Figure 1E**). Given that very few bands are present

156   in the control sample (DMSO, **Figure 1E**), the bands detected after MLN4924 treatment are

157   likely to be very labile isoforms of the NICD peptide, which are rapidly degraded in the DMSO

158   sample. In contrast, when whole cell lysate was treated with both MLN4924 and λ

159   phosphatase only one band, of the lowest molecular weight, was detectable, further supporting

160   the notion that the ladder of bands obtained upon MLN4924 treatment reflects a variety of

161   unstable phosphorylated NICD isoforms, which is completely depleted in the presence of λ

162   phosphatase (**Figure 1E**). As expected from data showing NICD levels are increased after

163   inhibitor treatment (**Figures 1A-D**), all three kinase inhibitors Roscovitine, DRB and XAV939

164   cause a noticeable increase in the number and intensity of bands compared to control cells.

165   However, compared to the effect seen with MLN4924, phos-tag technology reveals

166   Roscovitine, DRB and XAV939 have a reduced number of phospho-bands as compared to

167   MLN4924, indicative of the fact these kinase inhibitors act to reduce NICD phosphorylation.

168   Moreover, each of the inhibitors presents a distinct profile of NICD phospho-species. These

169   data suggest that NICD is targeted by several kinases and/or phosphorylation events which

170   are differentially sensitive to these inhibitors (**Figure 1E**).

171   NICD-FBXW7 interact at the endogenous levels in HEK293 cells, in a phosphorylation-

172   dependent manner. The involvement of the F-box protein component of the SCF E3 ligase

173   complex, FBXW7, in NICD degradation has been previously reported [46-48]. However, to

174   date, the NICD-FBXW7 interaction has only been shown in overexpressed systems [35, 44,

175   46, 63-66] Thus, we examined the binding of NICD to FBXW7 using co-immunoprecipitation

176   analysis at the endogenous level.

177   FBXW7 was immunoprecipitated from HEK293 cells treated with DMSO or MLN4924 for 3

178   hours and extracts were probed with NICD antibody. NICD directly binds to FBXW7 (**Figure

179   2A**). After MLN4924 treatment, the amount of NICD bound to FBXW7 was significantly higher

180   compared to control cells and this was particularly evident with the higher molecular weight

181   isoform of NICD (**Figures 2A-B**), confirming again NICD-FBXW7 interaction is

182   phosphorylation-dependent.

183   In order to determine if the change in the NICD phosphorylation profile observed after

184   treatment with the CDK inhibitors reduced the NICD-FBXW7 interaction, we performed the

185   same co-immunoprecipitation assay after CDK inhibitor treatment. In order to maximise the

186   amount of NICD immunoprecipitated with FBXW7, cells were treated with MLN4924 (to

187   prevent NICD degradation) in the presence or absence of the CDK inhibitors. A significantly

188   reduced interaction between NICD and FBXW7 was observed after treating HEK293 cells with

189   Roscovitine or DRB for 3 hours (**Figures 2C and 2E**). Statistical analyses, carried out on the

190   density of western blot bands after immunoprecipitation, confirmed a significant reduction in

191   the interaction between NICD and FBXW7 following either Roscovitine or DRB treatment

192   (**Figures 2D and 2F**).

193   Taken together, these data demonstrate, for the first time, that NICD interacts with FBXW7 at

194   endogenous levels in HEK293 cells, and this interaction is dependent on phosphorylation.

195   To further validate the involvement of FBXW7 in endogenous NICD turnover, we conducted a

196   siRNA-mediated depletion of FBXW7 in HEK293 cells (**Figure 2G**). siRNA treatment efficiently

197   depleted FBXW7 protein levels and led to an increase in levels of the FBXW7 target protein

198   Cyclin E. FBXW7 depletion also resulted in increased levels of NICD, and, in particular, an

199   accumulation of the phosphorylated form of NICD (**Figure 2G**).

200

201   **Serine 2513 is essential for the NICD-FBXW7 interaction**

202   We utilised Mass Spectrometry as an unbiased approach to identify which NICD residues are

203   phosphorylated in HEK293 cells transiently transfected with human NICD-GFP, followed by

204   immunoprecipitation of NICD-GFP. Gel slices were processed and submitted to MS analysis.

205   We identified 15 phospho-sites on exogenous hNICD, highlighted in green in **Figure 3A**. To

206   investigate the relevance of those phosphorylation sites in NICD turnover, we screened those

207   located within the PEST domain (such as S2527), and others based on the FBXW7 phospho-

208   degron motif (such as S2205, S2513, S2516, S2538) which is known to be [RK] S/T P [RK] X

209   S/T/E/D, where X is any amino acid and RK is any amino acid except arginine (R) or lysine

210   (K) [67].

211   Thus, we generated 5 peptides each carrying a serine to alanine point mutation in an identified

212   site. Following transient transfection of HEK293 cells with wild-type or mutated peptides we

213   performed immunoprecipitation using GFP-conjugated beads, to evaluate peptide binding

214   efficiency with endogenous FBXW7.

215   In 2004, Fryer and colleagues proposed that CDK8 phosphorylates serine residues 2481,

216   2484, 2506 (2513, 2516, 2538 in our annotation). They reported that when all of these residues

217   were mutated from serine to alanine, *in vitro* phosphorylation by recombinant CyClinC:CDK8

218   was dramatically reduced [35], suggesting these sites could be implicated in NICD stability.

219   However, we find individual mutations on serine residues 2205, 2516, 2527 and 2538 did not

220   affect the NICD-FBXW7 interaction (**Figure 3B, Supplementary Figure 3**). However,

221   mutating serine 2513 to alanine, to render this residue non-phosphorylatable, completely

222   abolished the NICD-FBXW7 interaction (**Figure 3B**). Cells transfected with the double mutant

223   S2513A/S2516A also showed a dramatic loss of the NICD-FBXW7 interaction. This did not

224   reflect a reduction in the level of immunoprecipitated GFP (**Figure 3B**).

225   Thus, our data suggest that only serine 2513, of those we have tested, is the key NICD

226   phosphorylation site required for interaction with FBXW7, and thus potentially crucial for NICD

227   stability and turnover.

228

229   **Cyclin Dependent Kinase (CDK) 1 and 2 phosphorylate NICD *in vitro***

230   Previous reports have proposed a number of potential kinases which may be involved in NICD

231   phosphorylation and turnover, including CyclinC:CDK8 [35], CyclinC:CDKs [65] and GSK3β

232   [34, 36]. The MRC-PPU Kinase Profiling Inhibitor Database (http://www.kinase-

233   screen.mrc.ac.uk/kinase-inhibitors) (University of Dundee) indicates that, at the

234   concentrations used in our assays, Roscovitine, in particular, is a potent inhibitor of CDK2, but

235   a very weak inhibitor of CK1, GSK3β and more than 50 other kinases tested. In order to

236 confirm results derived from the Kinase Profiling Inhibitor Database, we performed a kinase

237 assay in collaboration with the MRC-PPU International Centre for Kinase Profiling. We tested

238 three NICD phospho-peptides against the activity of a panel of different kinases including

239 CDK1 and CDK2 (**Table 1**). Of seven kinases tested, 5 had no specific activity against any of

240 the peptides. In contrast, CDK1 and CDK2 elicited a very high activity against Peptide 1, which

241 contained serine residues 2513 and 2516, previously identified by Mass spectrometry analysis

242 to be phosphorylated in NICD and in particular 2513 we have shown to be crucial for the NICD-

243 FBXW7 interaction.

244 These results demonstrate that CDK1 and CDK2 phosphorylate the C-terminal region of NICD

245 *in vitro*. Therefore, we decided to evaluate the contribution of these kinases to endogenous

246 NICD turnover and FBXW7 interaction in the cell lines. CDK2 siRNA treatment in HEK293

247 cells efficiently depleted CDK2 protein levels, with no effect on levels of CDK4. Under these

248 conditions NICD levels were significantly increased compared to control scrambled siRNA

249 treated cells, indicative of reduced NICD turnover (**Figures 4A-B**).

250 We repeated this assay and depleted CDK1 by a siRNA-mediated approach in HEK293 cells.

251 Under these conditions we also observed an increase in NICD protein levels compared to the

252 control (**Figure 4C**), and this increase was statistically significant (**Figure 4D**).Interestingly,

253 we also detected elevated levels of CDK2 and CDK8 following CDK1 depletion, suggesting a

254 possible compensation effect was occurring upon CDK1 knockdown. Nevertheless, this did

255 not prevent the effect of loss of CDK1 upon NICD turnover.

256 CDK8 has previously been proposed as a potential kinase involved in NICD phosphorylation

257 and turnover [35, 65]. We monitored NICD levels following efficient siRNA-mediated depletion

258 of CDK8 in HEK293 cells. This resulted in very slightly elevated NICD levels (**Figures 4E-F**).

259 These data suggest CDK8 may also phosphorylate NICD and regulate its turnover as

260 previously proposed [35, 65].

261 Taken together, these data provide further validation of CDK1 and CDK2 involvement in NICD

262 phosphorylation and turnover.

263

264 **Pharmacological inhibition of CDK2 and CDK1 activity increases levels of NICD *in vitro***

265 As a complementary approach to siRNA-mediated loss of function, we selected two small

266 molecule inhibitors that have a highly selective inhibitory activity against CDK2 kinase:

267 (Purvalanol B and GSK650394A). The specificity of each of these kinase inhibitors has been

268 tested (at two different concentrations) by the International Centre for Kinase profiling within

269 the MRC Protein Phosphorylation Unit at the University of Dundee. At 1 and 10 µM,

270 Roscovitine specifically inhibits more than 96% of CDK2 activity. Purvalanol B inhibits more

271 than 95% CDK2 activity, at 0.1 and 1 µM. GSK650394A inhibits 99% of CDK2 activity at both

272 1 and 10 µM (**Figure 5A**). CDK2 is by far the most sensitive target for all three inhibitors

273 (**Figure 5A**). HEK293 cells treated with Roscovitine, Purvalanol B or GSK650394A (10 µM,

274 0.1 µM and 10 µM, respectively) for 3 hours exhibited significantly increased NICD levels

275 compared to control DMSO treated cells (**Figures 5B-C**). Under these conditions protein

276 levels of both CDK2 and Cyclin E were not affected (data not shown). iPS cells cultured 3

277 hours in the presence of 0.1 µM Purvalanol B also exhibited significantly elevated levels of

278 NICD as compared to DMSO treated control cells, indicating this is a conserved effect of CDK2

279 (**Supplementary Figures 4A-B**).

280 Given our observation that both CDK1 and CDK2 can phosphorylate NICD peptides *in vitro*,

281 we similarly treated HEK293 cells with a CDK1 specific inhibitor, RO-3306 [68]. Following

282 exposure to 10 µM of RO-3306 for 3 hours HEK293 cells showed elevated NICD levels

283 compared to control DMSO treated cells (**Figures 5D-E**). These data further support the

284 hypothesis that both CDK1 and CDK2 are likely to be involved in phosphorylation-mediated

285 regulation of NICD turnover.

286

287 **NICD levels fluctuate over the cell cycle**

288 It is well known that CDK1 and CDK2 share several substrates, with a consequent functional

289 redundancy [69]. Our data demonstrate that these two kinases can phosphorylate NICD *in*

290 *vitro* and in the absence of either kinase NICD levels increase in HEK293 cells suggesting

291 they are not acting redundantly in this context. In order to further test this, we analysed whether

292 NICD levels fluctuate during the cell cycle where the role of both CDK1 and CDK2 has been

293 extensively reported in regulating transition to distinct cell cycle phases [70].

294 To that end, we synchronised HEK293 cells by using a double thymidine block assay. After

295 releasing from the second thymidine block, cells were collected at indicated time points and

296 cell cycle characterization was performed by Fluorescence Activated Cell Sorting (FACS)

297 (**Figure 6A**). **Figure 6A** shows the distribution though the cell cycle of HEK293 cells after

298 synchronization at early S-Phase (0 hour), as previously reported [71]. Two and four hours

299 post release, the majority of cells were in S-phase. At six hours post release, the majority of

300 cells were in G2 phase, while eight hours after release, the majority of cells were in late

301 G2/early M phase. At ten hours post release, the majority of cells had exited mitotic phase and

302 already entered G1. After twelve hours from release, cells were in mid/late G1 of the new cell

303 cycle (**Figure 6A**). The graph in **Figure 6B** represents the cell cycle distribution of HEK293

304 cells at distinct time points post double thymidine block and release from three independent

305 experiments analysed by FACS. Western blotting analysis of synchronized HEK293 cell

306 extracts showed the expression of several cell cycle regulatory proteins at the same distinct

307 time points reflecting distinct cell cycle phases as described above (**Figure 6C**). Interestingly,

308 we found that NICD levels fluctuated in a striking manner during the cell cycle, whereas we

309 saw no change to levels of FBXW7. At 2, 4, 8 and 12 hours post release, we observed a

310 dramatic decrease of NICD expression corresponding to CDK2-dependent G1/S phase,

311 whereas the decrease 8 hours after double thymidine block release occurred in the CDK1-

312 dependent G2/M phase transition. These data suggest that NICD levels fluctuate during the

313 cell cycle in a CDK1 and CDK2-dependent manner.

13

314   In addition, we analysed the cell cycle distribution by FACS in HEK293 cells after CDK2-siRNA

315   mediated depletion, which we have shown leads to a significant increase in NICD levels

316   (**Figure 4A**) and we observed a statistically significant accumulation of cells in G1 phase

317   compared to the control, as expected for cells deprived of CDK2 activity and therefore unable

318   to pass the G1/S checkpoint (**Figures 6D-E**). These data suggest that the drop in NICD levels

319   occurring in G1/S phase is due to CDK2 phosphorylation of NICD.

320

321   **Pharmacological inhibition of CDK2 increases NICD levels and delays the pace of the**

322   **segmentation clock in mouse PSM explants**

323   In order to address whether CDK2 phosphorylation of NICD is involved in driving the NICD-

324   FBXW7 interaction, we performed a co-immunoprecipitation assay with FBXW7 antibody and

325   analysed NICD by western blot after CDK2 inhibitor treatment. As above, in order to maximise

326   the amount of NICD immunoprecipitated HEK293 cells were treated with MLN4924 (to prevent

327   NICD degradation) +/- Purvalanol B (0.1 µM). A significantly reduced interaction between

328   NICD and FBXW7 was observed after treating HEK293 cells with Purvalanol B for 3 hours.

329   This did not reflect a reduction in the level of immunoprecipitated FBXW7 (**Figure 7A**).

330   Statistical analysis on the density of western blot bands after immunoprecipitation, confirmed

331   an extremely significant reduction in the NICD-FBXW7 interaction following Purvalanol B

332   treatment (**Figure 7B**).

333   In order to address the potential *in vivo* role of CDK-mediated NICD phosphorylation during

334   somitogenesis, we cultured E10.5 mouse PSM explants for 4 hours in the presence of 1µM of

335   Purvalanol B. Initially we analysed NICD levels by western Blot and just as in the *in vitro*

336   context, CDK2 inhibition resulted in increased NICD levels as compared to control embryos

337   (**Figure 7C**). This provides the first *in vivo* evidence CDK2 is likely to be involved in NICD

338   turnover.

339   Previous reports have suggested perturbations to NICD turnover leading to increased NICD

340   levels/stability are closely linked to an increase in the period of segmentation clock oscillations

341   in the PSM [18]. To further explore whether clock gene oscillations were delayed following

14

342   CDK2 inhibition, we used the half-embryo assay, where the PSM from one half of an E10.5

343   mouse embryo is cultured in control media, while the contralateral half from the same embryo

344   is cultured in the presence of 1µM of Purvalanol B for 4 hours. In 55.5% of cases examined

345   (n=10/18), exposure of PSM explants to Purvalanol B caused a delay in the pace of oscillatory

346   *mLfng* expression across the PSM as compared to the control explant (**Figure 7D**). Also, in

347   some cases the treated explant ("+") developed one somite less compared to the control

348   (**Figure 7D**).

349   Additionally, we cultured E10.5 mouse PSM explants in the presence or absence of the CDK1

350   inhibitor, RO-3306, for 4 hours at 10µM. Analysis of NICD levels by western blot revealed that

351   inhibition of CDK1 leads to elevated levels of NICD compared to control embryos (**Figure 7E**).

352   E10.5 mouse half embryo explants exposed to RO-3306 treatment for 4 hours showed

353   delayed clock oscillations of *mLfng* as compared to DMSO treated contralateral half embryo

354   explants (**Figure 7F**). These data, not only support our *in vitro* findings, but importantly

355   provide, for the first time, the *in vivo* evidence that CDK1 and CDK2 are involved in NICD

356   stability and turnover and that this molecular regulation of NICD turnover is extricably linked

357   to the pace of the segmentation clock.

358

359   **Mathematical model links NICD regulation and cell cycle**

360   To understand how our findings on the molecular details of NICD regulation in individual cells

361   give rise to tissue-scale delay of the segmentation clock, we first developed a mathematical

362   model of NICD production and degradation in HEK293 cells. The variables in the model define

363   the position of a cell in the cell cycle, the amount of NICD and the amount of phosphorylated

364   NICD (pNICD) at time t. The model enables us to connect assumptions about molecular

365   processes in individual cells with experiments performed on a large population of cells.

366   We assume a K-compartment model that describes sequential progression of a cell through

367   the cell cycle (**Figure 8A**). It is assumed that CDKs that phosphorylate NICD, resulting in its

368   interaction with FBXW7 and subsequent degradation, are active in some m of the cell cycle

369   states. We assume that: (i) NICD exists in non-phosphorylated and phosphorylated forms; (ii)

15

370   NICD is produced at constant rate k_1; (iii) both forms of NICD get degraded at background

371   rate k_7; (iv) NICD gets phosphorylated by CDKs at rate k_3; (v) pNICD degrades at rate k_6 with

372   $k_6 > k_7$; and (vi) dephosphorylation of NICD occurs at rate k_2. We consider the

373   pharmacological perturbations as follows: LY411575 treatment experiments, in which NICD

374   production is inhibited, are simulated by setting $k_1 = 0$; Purvalanol B/Roscovitine treatment

375   experiments, which target only CDK2, reduce the number of compartments where CDKs are

376   active by a factor of two; and MLN4924 treatment, which inhibits FBXW7 mediated

377   degradation of NICD, are simulated by removing the fast mode of decay ($k_6 = 0$).

378   By averaging cellular descriptions of NICD and the cell cycle over a given cell population, we

379   derive equations describing the average levels of total NICD (i.e. as measured in a Western

380   Blot experiment, see Methods). Upon release from double thymidine block, cells are

381   synchronised in the cell cycle and there are relatively high levels of CDK activity at different

382   times post release. As pNICD degrades faster, high levels of CDK results in lower levels of

383   NICD (see **Figure 8** and **Figures 4A-D, 5B-E, 6C, 7C-E**). We find the model qualitatively fits

384   the experimental observations if NICD is phosphorylated in two separate time windows post

385   release. We propose that these windows correspond to activity of CDK2 (G1/S phase) and

386   CDK1 (M phase) (**Figures 8A** and **8B**). In a situation where the cell cycle is desynchronised,

387   the population-averaged phosphorylation rate (mk_3/K, where m/K is the fraction of the cell

388   cycle where CDKs are active) is a fraction of the true phosphorylation rate. The model can

389   reproduce Western Blot results from DMSO and MLN4924 experiments (**Figure 8C**), allowing

390   inference of the parameters k_2 and k_3. Notably, the simulated Purvalanol B/Roscovitine

391   treatment experiment presented in Figure 8C is a prediction that is validated by the

392   experimental data.

393   To explore how CDK inhibition results in delay of the segmentation clock we introduce an

394   additional variable representing phase of the somitogenesis clock and assume that the caudal

395   PSM behaves like a population of phase coupled oscillators. In Wiederman et al. we proposed

396   a model that showed how competition between activators and inhibitors of clock gene

16

397   transcription could lead to the oscillator period being an increasing function of NICD half-life

398   [18]. Here, we impose, without explicitly describing the molecular circuitry, this assumption.

399   We assume that each cellular oscillator has a natural frequency $\omega_i(t)$ that is a function of cell

400   cycle position; when CDKs are active the baseline clock frequency, ω_0, is increased by an

401   acceleration factor r (**Figure 8D**). As the cell cycle is asynchronous in the PSM, it is therefore

402   comprised of a population of oscillators with frequencies ω_0 or ωr_0. Given sufficiently strong

403   coupling a population of such oscillators yields synchronous oscillations with a period that is

404   an average of the individual oscillator periods (**Figures 8E-8F**). Upon CDK inhibition, the

405   relative number of faster oscillators is reduced hence the average period decreases (**Figure

406   8E**). Hence the cell cycle somitogenesis coupled model provide a mechanistic description of

407   how CDK-mediated phosphorylation of NICD can result in the observed phenotype in PSM

408   tissue (**Figure 7**).

17

DISCUSSION

The Notch pathway plays multiple critical roles in somitogenesis. Notch signalling is critical for dynamic clock gene expression and for somite formation in mice [9]. Notch-Delta signalling is essential to synchronise clock gene oscillations among neighbouring cells of the PSM [10-13]. Moreover, a recent publication using a pharmacological approach, has shown that modulating the half-life of NICD affects the clock oscillation period and somite size [18]. It is important to note that NICD degradation and turnover still occurred under these conditions but less efficiently. In this study, we have significantly extended those findings to determine the mechanistic details of regulation of NICD turnover, and we report for the first time that cell cycle-dependent CDK1 and CDK2 activity is involved in NICD turnover, which has broad implications across all developmental and disease contexts where Notch plays a role.

We demonstrate that kinase inhibitors (Roscovitine, DRB and XAV939), previously shown to prolong NICD half-life and delay the segmentation clock pace in mouse and chick PSM *in vivo*, [18] also increased endogenous levels of human NICD when a range of primary human cell lines were treated for 3 hours. This highlights the conserved effect of these inhibitors on regulating NICD stability, which is perhaps not surprising given the high degree of sequence similarity between mouse, human and chicken NICD.

We demonstrate that, following exposure to these kinase inhibitors, the increased stability of NICD accompanies a change in the array of phosphorylated isoforms of NICD observed. The different profiles of phosphorylated isoforms of NICD observed, following exposure to each of the inhibitors, suggest they each inhibit distinct kinases. In each case, however, the highest molecular bands were no longer visible. It is possible that the multiple phosphorylation bands are indicative of unique events, some of which may reflect priming phosphorylation events that facilitate or increase the efficiency of secondary phosphorylation events, which then act as phospho-degron signals to recruit E3 ligases that target NICD for degradation. It is not possible to determine whether the lower molecular weight bands that remain, following inhibitor treatment, are indicative of the loss of primary or secondary phosphorylation events.

437   A number of reports have highlighted the fact that the SCF[FBXW7] E3 ligase plays an important

438   role in NICD degradation [35, 44, 46-48, 66]. SCFs (Skp1, Cullin-1, F-box protein) are a class

439   of E3 ligases that use Cullin-1 as a scaffold and F-box proteins as substrate receptors. FBXW7

440   is an evolutionary conserved F-box protein. Substrate phosphorylation instigates FBXW7

441   binding to a conserved CDC4 phospho-degron motif which then recruits the rest of the E3

442   ligase complex, including Cullin1, thereby targeting the substrate for ubiquitination and

443   subsequent degradation by the proteasome [45, 49]. The role of FBXW7 in NICD regulation

444   is also supported by data showing that, when mammalian Sel-10 (homologue of FBXW7 in *C.*

445   *elegans*) is mutated, NICD is much more stable [46]. To date, the interaction between NICD

446   and FBXW7 by co-immunoprecipitation has only been shown using overexpressed proteins,

447   due to the fact this interaction is very transient and leads to efficient degradation of NICD [35,

448   44, 47, 48, 66]. In order to stabilise the interacting complex, we conducted experiments in the

449   presence of MLN4924, a Cullin1 neddylation inhibitor which prevents activation of Cullin1.

450   Under these conditions, we demonstrate for the first time that NICD and FBXW7 can interact

451   at endogenous levels in HEK293 cells. Moreover, this allowed us to demonstrate that, when

452   phosphorylation is disrupted by small molecule CDK inhibitors (Roscovitine or DRB), the

453   NICD-FBXW7 interaction is reduced. It is important to note that neither inhibitor abolished the

454   NICD-FBXW7 interaction which suggests again that they are each inhibiting only some of the

455   kinase activity involved in NICD phosphorylation and subsequent recruitment of FBXW7. This

456   aligns with the observation that in the chick/mouse PSM both of these inhibitors increase NICD

457   stability and the period of the segmentation clock but that NICD turnover still occurs in this

458   tissue, and thus is dependent on a number of different kinases/phosphorylation events

459   differentially targeted by these two inhibitors [18].

460   By Mass Spectrometry analysis, we identified 15 phospho-sites within human exogenous

461   NICD in HEK293 cells, some of which have been previously identified and reported to be

462   involved with NICD turnover [35, 65]. Among those phospho-sites identified, we found that

463   Serine 2513, when mutated to alanine, thereby rendering the site non phosphorylatable, was

464   essential for the interaction between NICD and FBXW7. Point mutations in a number of other

19

465   phosphorylated residues showed these are non-essential for this NICD-FBXW7 interaction,

466   including two residues that have previously been reported to potentially be required for the

467   interaction; S2484 and S2506 (S2516 and S2538 in our annotation) [35, 66]. However, Fryer

468   and colleagues used exogenous proteins and mutated all three sites simultaneously so the

469   individual contribution/requirement of each residue was not addressed in that study. O'Neil

470   and colleagues have also reported, using exogenous proteins, that phosphorylation of the

471   Threonine residue at T2487 in mouse NICD (T2511 in our annotation) is key to driving the

472   NICD-FBXW7 interaction and subsequent ubiquitination of NICD [44]. We did not observe

473   phosphorylation at this residue in human NICD. However it would be interesting to repeat the

474   mass spec analysis using different enzyme digestions to determine if this reveals additional

475   phosphorylated sites that play a role in this interaction.

476   SCF substrates typically have many phospho-degrons that can be widely dispersed. It will be

477   important to test the requirement of all the phosphorylated residues we have identified in NICD

478   for driving and regulating the NICD-FBXW7 interaction.

479   We have identified CDK1 and CDK2 as two kinases that can phosphorylate NICD in the PEST

480   region that harbours residue serine 2513, which we have demonstrated to be crucial for the

481   interaction between NICD and FBXW7. Through two loss of function approaches, namely

482   siRNA and a pharmacological approach, we further demonstrated the role of both CDK1 and

483   CDK2 kinases in the regulation of NICD turnover. Indeed, by transfecting HEK293 cells with

484   CDK1, or CDK2 specific siRNA, or treating HEK293 cells or iPS cells with highly selective

485   small molecule inhibitors against CDK1 and CDK2, we could appreciate an increase in NICD

486   levels, indicating that inhibiting phosphorylation by CDK1 or CDK2, renders NICD more stable.

487   As described above, the serine 2513 residue has previously been reported to potentially be

488   involved in NICD turnover in other systems [35]. Using gain and loss of function experiments

489   with exogenous proteins, the authors reported phosphorylation occurred through

490   CyclinC:CDK8. Indeed, by transfecting HEK293 cells with CDK8 specific siRNA, we could also

491   appreciate an increase in NICD levels, indicating that this kinase could also play a role in NICD

492   turnover, although the effect appears less dramatic compared to that observed with CDK1 or

493   CDK2 specific siRNA.

494   CDK1 and CDK2 activity and thus phosphorylation of their substrates changes in a cell cycle

495   dependent manner [72]. Strikingly, we find that NICD levels vary in HEK293 cells in a cell

496   cycle-dependent way such that we observe lowest levels of NICD in phases of the cell cycle

497   where CDK1/Cyclin B1 and CDK2/Cyclin E levels are highest and therefore when these

498   complexes are reported to be most active [73]. This finding suggests that NICD activity, signal

499   duration and signal strength is likely to vary in a cell cycle dependent manner, potentially

500   leading to differential transcriptional output in different phases of the cell cycle.

501   Given our findings, it is striking that CDK2 homozygous *null* mice are viable [74]. However, it

502   has been reported that CDK1 and CDK2 share more than 50% of their targets [75] which is

503   likely to allow for a lot of redundancy in this knock-out line, as CDK1 can compensate for loss

504   of CDK2 by forming active complexes with A-, B-, E- and D-type cyclins. The CDK1-*null*

505   homozygous mice however are embryonic lethal and a CDK2 knock-in to the CDK1 locus is

506   unable to rescue this phenotype [76, 77]. It would be interesting to examine the role of the

507   CDK1 conditional mutant in the context of Notch signalling and somitogenesis [78].

508   Interestingly, Cyclin C-*null* mice, which are embryonic lethal at 10.5, show dramatically

509   reduced NICD1 phosphorylation *in vivo*, and elevated NICD1 levels. The authors show that

510   Cyclin C can complex with CDK3, CDK19, CDK8, CDK1 and CDK2 to phosphorylate NICD1

511   and promote NICD1 degradation [65]. Thus, it would be very interesting to examine a PSM

512   conditional Cyclin C loss of function to determine whether this cyclin is involved in regulating

513   NICD turnover in this tissue. It is noteworthy Cyclin C levels did not appear to vary in a cell

514   cycle dependent manner in HEK293 cells, although it is possible the activity of Cyclin C/CDK

515   complexes varies in a cell cycle-dependent manner through post-translational modifications

516   rather than protein levels per se.

517   The finding that CDK1 inhibition or CDK2 inhibition leads to increased levels of NICD in E10.5

518   mouse embryo PSM lysates and to a delay in clock gene oscillations and somite formation

519   provides the first *in vivo* evidence that both CDK1 and CDK2 are involved in NICD turnover.

21

520   It is noteworthy that inhibition of CDK2 activity with a highly selective inhibitor reduces the

521   NICD-FBXW7 interaction in HEK293 cells but does not block it completely, as we saw with

522   Roscovitine and DRB. Indeed, inhibition of CDK1 or CDK2 in the mouse PSM with highly

523   selective inhibitors raises NICD levels and also slows, but does not block, dynamic Notch

524   target clock gene expression, and somitogenesis. This suggests that some NICD turnover

525   persists under these conditions, possibly through redundancy between CDK1 and 2 and/or

526   through CDK8-mediated phosphorylation, the subsequent recruitment of E3 ligases and

527   degradation of NICD. Moreover, a report by Chiang *et al.* has also identified a region

528   downstream of the PEST sequence, termed S4, that is involved in NICD degradation, but that

529   is independent of FBXW7 activity [79]. These data indicate there are several mechanisms

530   regulating NICD turnover which are partially redundant.

531   We also developed a mathematical model that coupled cell cycle dynamics to NICD

532   degradation. Using HEK293 cells, model parameters were identified that recapitulated the

533   distributions of cells in the different cell cycle phases. To recover qualitative features of NICD

534   thymidine release experiments, NICD phosphorylation was required at distinct stages in the

535   cell cycle. After using MLN4924 and control experiments to estimate NICD phosphorylation

536   rate the model qualitatively predicts the effect of Roscovitine/PurB treatment on total NICD

537   levels. To address the likely effect of CDK2 inhibition in the PSM, the model was extended to

538   account for position of a cell in the segmentation clock cycle. Following Wiederman *et al.* [18],

539   it was assumed that levels of NICD are anti-correlated with clock somitogenesis frequency.

540   Hence, the posterior PSM is represented by a population of phase coupled oscillators whose

541   frequency is cell cycle dependent. Simulating CDK2 inhibition removes a pool of faster

542   oscillators thus reducing the tissue period.

543   Notch plays a key role as a gatekeeper protecting progenitor and/or stem cells in multiple

544   developmental contexts, in part through preventing differentiation and in part through

545   regulating components of the cell cycle [80-82]. Our novel finding of a reciprocal auto-

546   regulatory role between the cell cycle regulated CDKs, CDK1 and CDK2, and NICD turnover

22

547   has potentially great relevance to the developmental biology community and may provide

548   additional insight into disease/cancer contexts where this autoregulation may have gone awry.
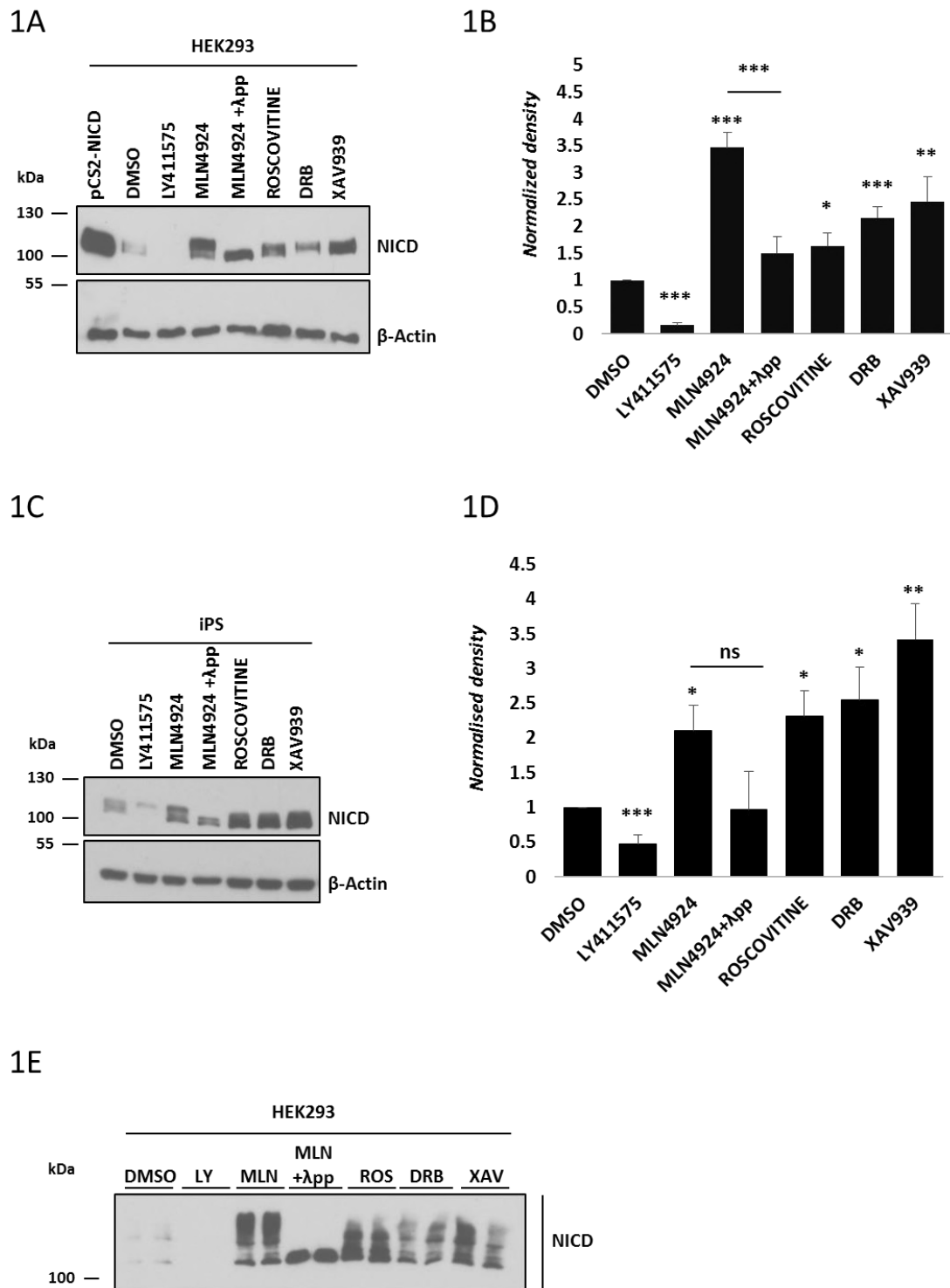
Figure 1

Figure 1. Endogenous NICD levels increase in HEK293 cells following treatment with Roscovitine, DRB and XAV939.

(A) HEK293 cells were treated for 3 hours with 150 nM of LY411575, 1 µM of MLN4924, 10 µM of Roscovitine, 10 µM DRB or 10 µM XAV939. DMSO served as vehicle control.

24

556   Transfection with pCS2-NICD vector served as positive control. Western blot analysis reveals

557   that NICD levels were increased upon treatment with Roscovitine, DRB, XAV939, or

558   MLN4924. NICD is undetectable following LY411575 treatment. NICD antibody detects a

559   doublet following inhibitor treatment and the top band disappears following λ phosphatase

560   treatment indicating that this top band is a phosphorylated isoform. β-Actin served as loading

561   control.

562   (B) Quantification of the density of western blot bands in (A) using ImageJ software. Data are

563   expressed as fold changes compared to DMSO treatment. All data represent the mean ± SEM

564   from three independent experiments. Student's t-test analysis was performed with *$p \leq 0.05$,

565   **$p \leq 0.01$, ***$p \leq 0.001$.

566   (C) iPS cells were treated for 3 hours with 150 nM of LY411575, 1 µM of MLN4924, 10 µM of

567   Roscovitine, 10 µM DRB or 10 µM XAV939. DMSO has been used as vehicle control. Western

568   blot analysis reveals that NICD levels were increased upon treatment with Roscovitine, DRB,

569   XAV939, or MLN4924. NICD is undetectable following LY411575 treatment. NICD antibody

570   detects a doublet following Inhibitor treatment and the top band disappears following λ

571   phosphatase treatment indicative that this top band is a phosphorylated isoform. β-Actin

572   served as loading control.

573   (D) Quantification of the density of western blot bands in (C) using ImageJ software. Data are

574   expressed as fold changes compared to DMSO treatment. All data represent the mean ± SEM

575   from three independent experiments. Student's t-test analysis was performed with *$p \leq 0.05$,

576   **$p \leq 0.01$, ***$p \leq 0.001$.

577   (E) HEK293 cells were treated with the same inhibitors as described in (A). NICD

578   phosphorylation status was analysed by a Phos-tag assay. DMSO served as vehicle control.

579   NICD phosphorylation profile varies following Roscovitine, DRB, XAV939 or MLN4924

580   treatment. Following λ phosphatase treatment none of the high molecular weight bands are

581   visible indicating they are all phosphorylated isoforms.
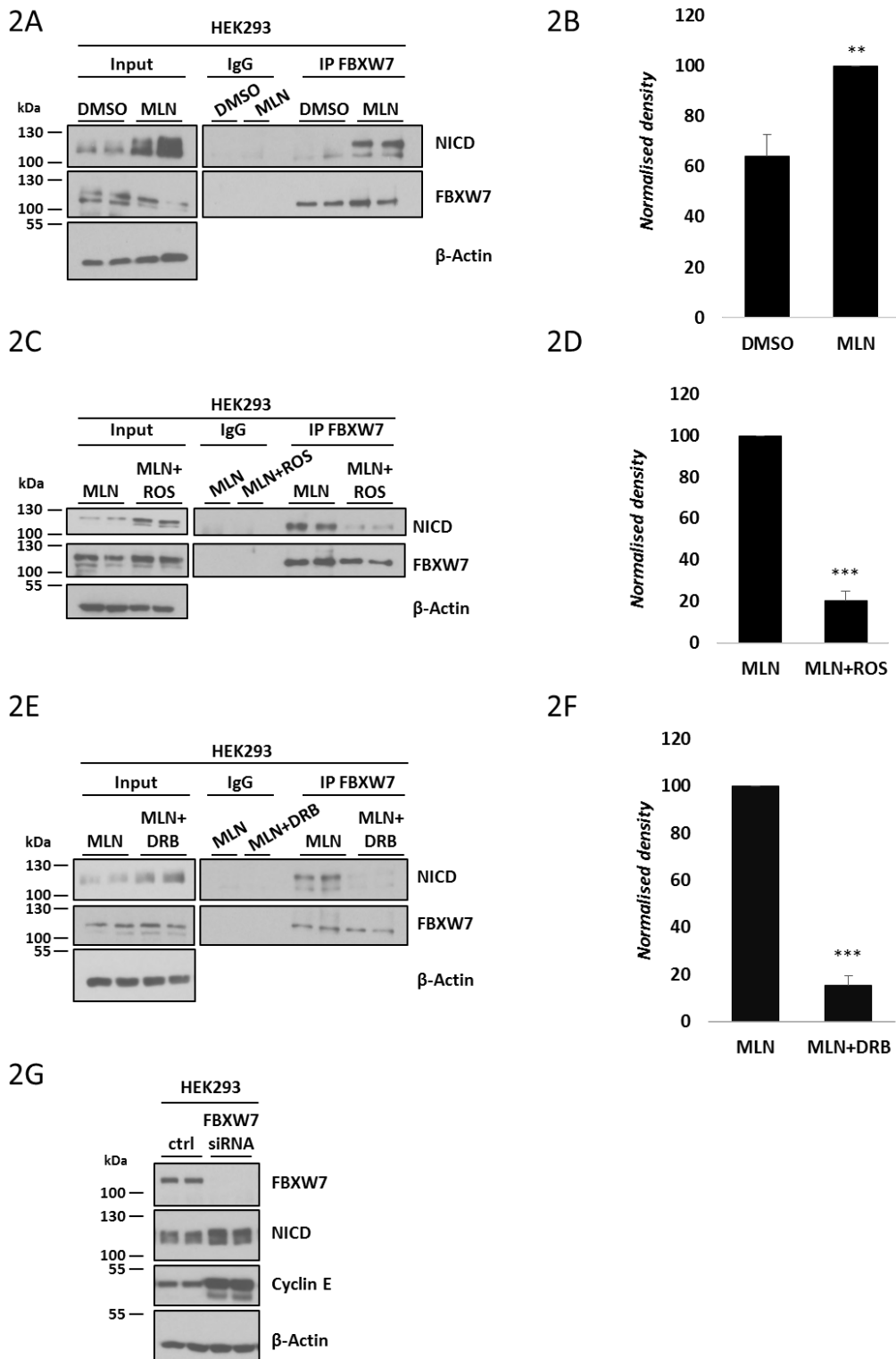
Figure 2

Figure 2. **NICD and FBXW7 interact directly at endogenous levels.**

(A) NICD interaction with FBXW7 at endogenous levels in HEK293 cells. 500 µg of HEK293

cell lysates treated with DMSO or MLN4924 were subjected to immunoprecipitation using

588   FBXW7 antibody, or IgG antibody as negative control, and precipitated material was analysed

589   by western blot using NICD antibody. Western blot with FBXW7 antibody served as loading

590   control for immunoprecipitation efficiency. 10% of cell lysate before immunoprecipitation was

591   used as input control and β-Actin served as loading control.

592   (B) Quantification of the density of western blot bands in (A) performed by ImageJ software.

593   Data are expressed as fold changes compared to DMSO. All data represent the mean ± SEM

594   from three independent experiments. Student t-test was used to determine p values, with

595   **p≤0.01.

596   (C) Roscovitine treatment reduced the NICD-FBXW7 interaction. 500 μg of HEK293 cell

597   lysates treated with MLN4924 or MLN4924 together with Roscovitine were subjected to

598   immunoprecipitation using FBXW7 antibody, or IgG antibody as negative control, and

599   precipitated material was analysed by western blot using NICD antibody. Western blot with

600   FBXW7 antibody served as loading control for immunoprecipitation efficiency. 10% of cell

601   lysate before immunoprecipitation was used as input control and β-Actin served as loading
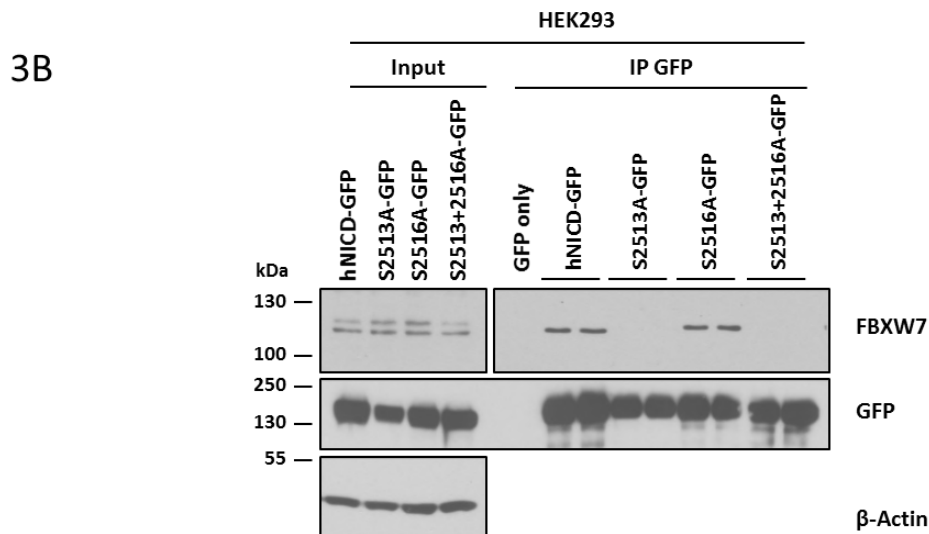
602   control.

603   (D) Quantification of the density of western blot bands in (C) performed by ImageJ software.

604   Data are expressed as fold changes compared to MLN4924 treated samples. All data

605   represent the mean ± SEM from three independent experiments. Student's t-test analysis was

606   performed, with ***p≤0.001.

607   (E) Interaction between NICD and FBXW7 is reduced following DRB treatment. 500 μg of

608   HEK293 cell lysates treated with MLN4924 or MLN4924 together with DRB were subjected to

609   immunoprecipitation using FBXW7 antibody, or IgG antibody as negative control, and

610   precipitated material was analysed by western blot using NICD antibody. Western blot with

611   FBXW7 antibody served as loading control for immunoprecipitation efficiency. 10% of cell

612   lysate before immunoprecipitation was used as input control and β-Actin served as loading

613   control.

614   (F) Quantification of the density of western blot bands in (E) performed by ImageJ software.

615   Data are expressed as fold changes compared to MLN4924 treated samples. All data

616   represent the mean ± SEM from three independent experiments. Student's t-test analysis was

617   performed, with ***p≤0.001.

618   (G) Inhibiting endogenous FBXW7 modulates endogenous NICD levels. HEK293 cells were

619   transfected with control (scrambled siRNA) or FBXW7 siRNA. Levels of FBXW7, NICD and

620   Cyclin E were determined by western blot. β-Actin served as loading control.

621 **Figure 3**

3A

```
            1760         1770         1780         1790         1800
     GCGVLLSRKR  RRQHGQLWFP  EGFKVSEASK  KKRREPLGED  SVGLKPLKNA
            1810         1820         1830         1840         1850
        SDGALMDDNQ  NEWGDEDLET  KKFRFEEPVV  LPDLDDQTDH  RQWTQQHLDA
            1860         1870         1880         1890         1900
        ADLRMSAMAP  TPPQGEVDAD  CMDVNVRGPD  GFTPLMIASC  SGGGLETGNS
            1910         1920         1930         1940         1950
        EEEEDAPAVI  SDFIYQGASL  HNQTDRTGET  ALHLAARYSR  SDAAKRLLEA
            1960         1970         1980         1990         2000
        SADANIQDNM  GRTPLHAAVS  ADAQGVFQIL  IRNRATDLDA  RMHDGTTPLI
            2010         2020         2030         2040         2050
        LAARLAVEGM  LEDLINSHAD  VNAVDDLGKS  ALHWAAAVNN  VDAAVVLLKN
            2060         2070         2080         2090         2100
        GANKDMQNNR  EETPLFLAAR  EGSYETAKVL  LDHFANRDIT  DHMDRLPRDI
            2110         2120         2130         2140         2150
        AQERMHHDIV  RLLDEYNLVR  SPQLHGAPLG  GTPTLSPPLC  SPNGYLGSLK
            2160         2170         2180         2190         2200
        PGVQGKKVRK  PSSKGLACGS  KEAKDLKARR  KKSQDGKGCL  LDSSGMLSPV
            2210         2220         2230         2240         2250
        DSLESPHGYL  SDVASPPLLP  SPFQQSPSVP  LNHLPGMPDT  HLGIGHLNVA
            2260         2270         2280         2290         2300
        AKPEMAALGG  GGRLAFETGP  PRLSHLPVAS  GTSTVLGSSS  GGALNFTVGG
            2310         2320         2330         2340         2350
        STSLNGQCEW  LSRLQSGMVP  NQYNPLRGSV  APGPLSTQAP  SLQHGMVGPL
            2360         2370         2380         2390         2400
        HSSLAASALS  QMMSYQGLPS  TRLATQPHLV  QTQQVQPQNL  QMQQQNLQPA
            2410         2420         2430         2440         2450
        NIQQQQSLQP  PPPPPQPHLG  VSSAASGHLG  RSFLSGEPSQ  ADVQPLGPSS
            2460         2470         2480         2490         2500
        LAVHTILPQE  SPALPTSLPS  SLVPPVTAAQ  FLTPPSQHSY  SSPVDNTPSH
            2510         2520         2530         2540         2550
        QLQVPEHPFL  TPSPESPDQW  SSSSPHSNVS  DWSEGVSSPP  TSMQSQIARI

        PEAFK
```

3B

622

623

624   **Figure 3**. **Mass spectrometry analysis of phosphorylated residues in hNICD**.

625   (A) LC-MS-MS analysis of in-gel-digested HEK293 cells transfected with hNICD-GFP, and

626   subjected to immunoprecipitation using GFP antibody, identified multiple phosphorylation sites

627   in NICD, highlighted in green.

628   (B) Phosphorylation of serine 2513, but not serine 2516, is required for the NICD-FBXW7

629   interaction. hNICD-GFP phospho-mutant peptides encoding non-phosphorylatable residues

630   at S2513 and/or 2516 (serine to alanine) were expressed in HEK293 cells. The exogenously

631   expressed protein was subsequently immunoprecipitated with anti-GFP antibody and

632   precipitated material was analysed by western blot using FBXW7 antibody. Wild-type hNICD-

633   GFP and GFP only vectors were included as positive and negative controls, respectively.

634   Western blot using GFP antibody served as immunoprecipitation efficiency control. β-Actin

635   has been used as loading control for the input lanes.

29

Table 1

Specific activity (U/mg)	Peptide 1	Peptide 2	Peptide 3	Control
Cdk1/CyclinA2	**1035.43**	35.21	-7.86	1322
Cdk1/CyclinB	**887.23**	37.46	0.04	1566
Cdk2/CyclinA	**79.7**	0.5	0	117.7
Cdk5/p35	47	0.8	0.5	1729.5
Cdk7/MAT1/CyclinH	0.1	0.2	0.1	21.6
Cdk9/CyclinT1	2.7	0.6	0.3	66.4
CK1α	0	0	0.1	19.1
GSKβ	1	1	1.1	552.5

Peptide 1: S2513 and S2516   HPFLTP**S**PE**S**PDQWSSSSPH
Peptide 2: S2538   NVSDWSEGVSS**S**PPTSMQSQIA
Peptide 3: S2141   GTPTLSPPLC**S**PNGYLGSLKP

Table 1. **CDK1 and CDK2 exhibit specific activity against a NICD phospho-peptide by *in vitro* kinase assay**. Three NICD phospho-peptides were tested for the activity of seven different kinases (CDK1, CDK2, CDK5, CDK7, CDK9, CK1α and GSKβ). A known substrate was used as control for each kinase. The specific activity of each kinase is expressed in *U/mg*. Peptide 1 contains serine residues 2513 and 2516 (HPFLTP**S**PE**S**PDQWSSSSPH). Peptide 2 includes serine 2538 (NVSDWSEGVSS**S**PPTSMQSQIA). Peptide 3 encompasses serine residue 2141 (GTPTLSPPLC**S**PNGYLGSLKP).

646   **Figure 4**
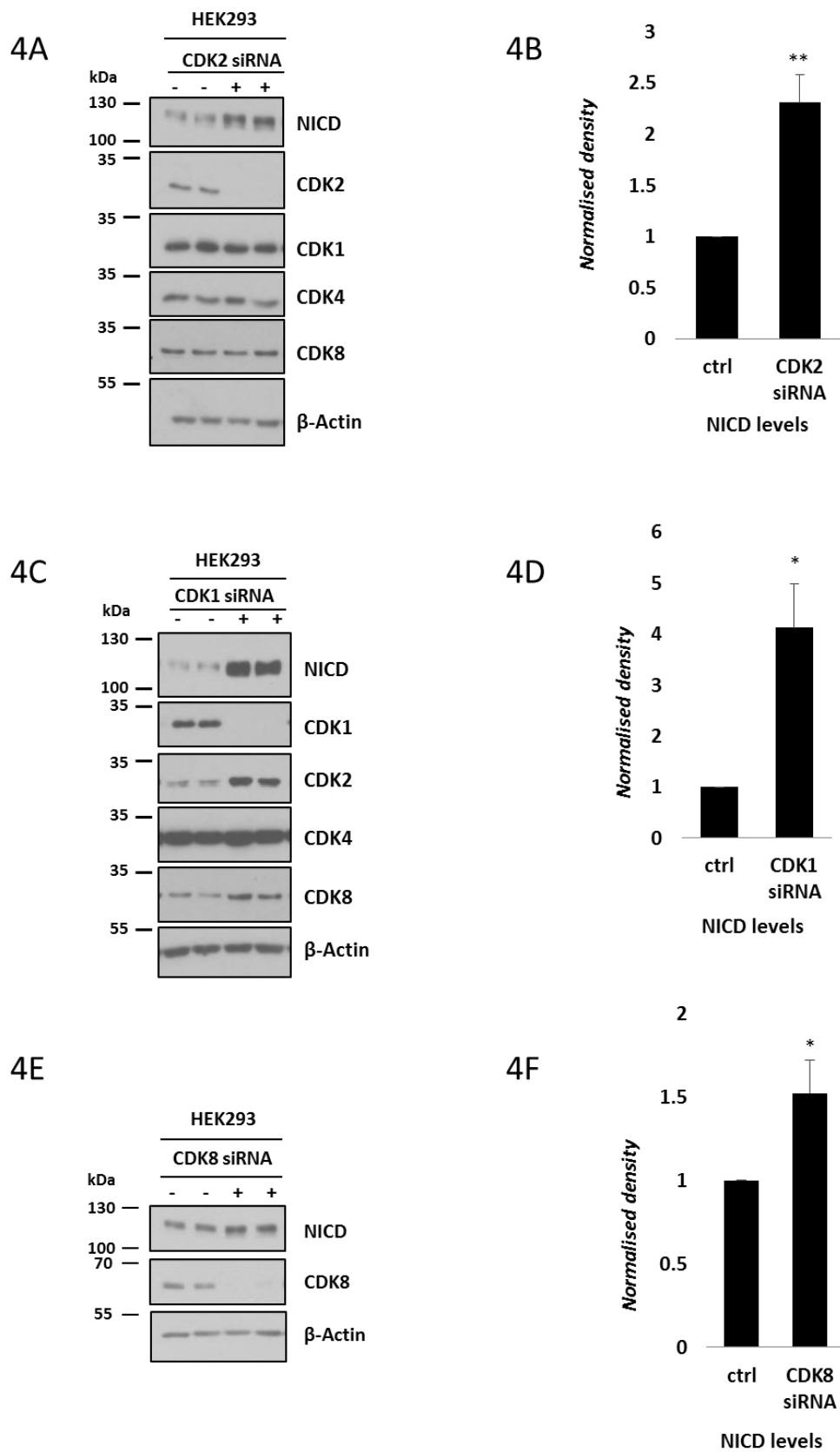
647

648 **Figure 4**. **CDK1, CDK2 and CDK8 depletion increased endogenous levels of NICD in**

649 **HEK293 cells**.

650 (A) HEK293 cells were cultured for 48h after transfection with plasmids encoding scrambled

651 siRNA (-) or siRNA specific for CDK2 (+) followed by western blot for NICD, CDK2, CDK1,

652 CDK4 and CDK8. β-Actin served as loading control.

653 (B) Quantification of the density of western blot bands in (A) performed by ImageJ software.

654 Data are expressed as fold changes compared to control (scrambled siRNA transfected) cell

655 lysate. All data represent the mean ± SEM from three independent experiments. Student's t-

656 test analysis was performed, with **p≤0.01.

657 (C) HEK293 cells were cultured for 48h after transfection with plasmids encoding scrambled

658 siRNA (-) or siRNA specific for CDK1 (+) followed by Western blot for NICD, CDK1, CDK2,

659 CDK4 and CDK8. β-Actin has been used as loading control.

660 (D) Quantification of the density of western blot bands in (C) performed by ImageJ software.

661 Data are expressed as fold changes compared to control (scrambled siRNA transfected) cell

662 lysate. All data represent the mean ± SEM from three independent experiments. Student's t-

663 test analysis was performed, with *p≤0.05.

664 (E) HEK293 cells were cultured for 48h after transfection with plasmids encoding scrambled

665 siRNA or siRNA specific for CDK8, followed by western blot for NICD and CDK8. β-Actin has

666 been used as loading control.

667 (F) Quantification of the density of western blot bands in (E) performed by ImageJ software.

668 Data are expressed as fold changes compared to control (scrambled siRNA transfected) cell

669 lysate. All data represent the mean ± SEM from three independent experiments. Student's t-

670 test analysis was performed, with *p≤0.05.

671 **Figure 5**

5A

	% activity remaining					
	Roscovitine		*Purvalanol B*		*GSK650394A*	
	1 µM	10 µM	0.1 µM	1 µM	1 µM	10 µM
CDK2-CyclinA	4	3	5	2	1	0
CK1	76	30	107	58	12	3
GSK3	76	102	91	62	78	23
CK2	92	102	101	62	82	46
CSK	88	103	96	75	96	98
ERK1	82	60	102	61	75	39
PLK1	91	73	106	69	31	5
CHK2	93	67	98	40	40	28

5B

5C

5D

5E

672

33
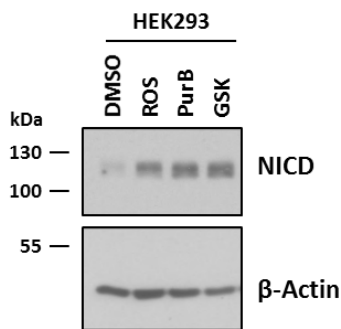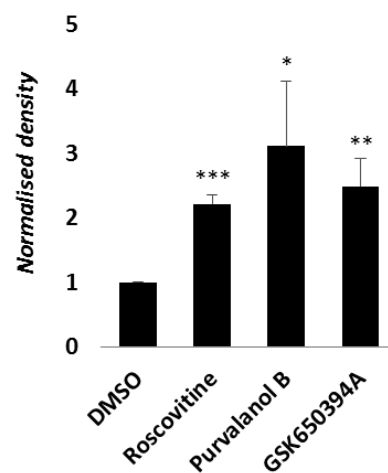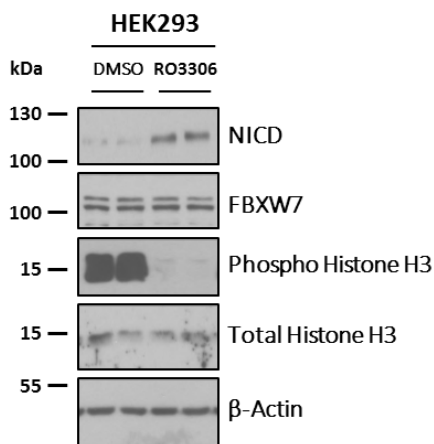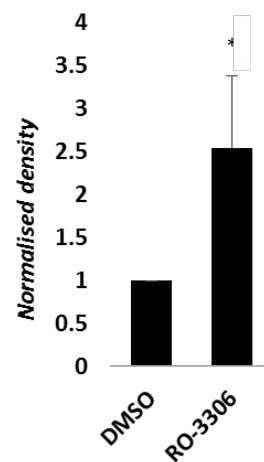
673 **Figure 5**. **Pharmacological inhibition of CDK1 and CDK2 leads to increased NICD levels**

674 *in vitro.* (A) Analysis of the inhibitory activity of three highly selective CDK2 inhibitors against

675 a panel of kinases - a selection of those tested is shown here. At both 1 and 10µM, Roscovitine

676 is able to inhibit more than 95% of CDK2 activity, but is far less effective against other kinases.

677 Purvalanol B (0.1 and 1µM) inhibits more than 94% of CDK2 activity. At both 1 and 10 µM,

678 GSK650394A is able to inhibit more than 98% of CDK2 activity. Source: The Kinase Profiling

679 Inhibitor Database (http://www.kinase-screen.mrc.ac.uk/kinase-inhibitors).

680 (B) HEK293 cells were treated with three highly selective CDK2 inhibitors (10 µM of

681 Roscovitine, 0.1µM of Purvalanol B and 10µM of GSK650394A) for 3 hours. Endogenous

682 levels of NICD were detected by western blot. β-Actin served as loading control.

683 (C) Quantification of the density of western blot bands in (B) using ImageJ software. Data are

684 expressed as fold changes compared to DMSO. All data represent the mean ± SEM from

685 three independent experiments. Student's t-test analysis was performed, with *p≤0.05,

686 **p≤0.01, and ***p≤0.001.

687 (D) HEK293 cells were treated with RO-3306, a specific CDK1 inhibitor, for 3 hours at 10 µM.

688 Levels of NICD, FBXW7, phospho-Histone H3 and Histone H3 were detected by western blot.

689 β-Actin was used as loading control.

690 (E) Quantification of the density of western blot bands in (D) using ImageJ software. Data are

691 expressed as fold changes compared to DMSO. All data represent the mean ± SEM from

692 three independent experiments. Student's t-test analysis was performed, with *p≤0.05.

Figure 6

6A

6B

6C

6D

6E

694

695
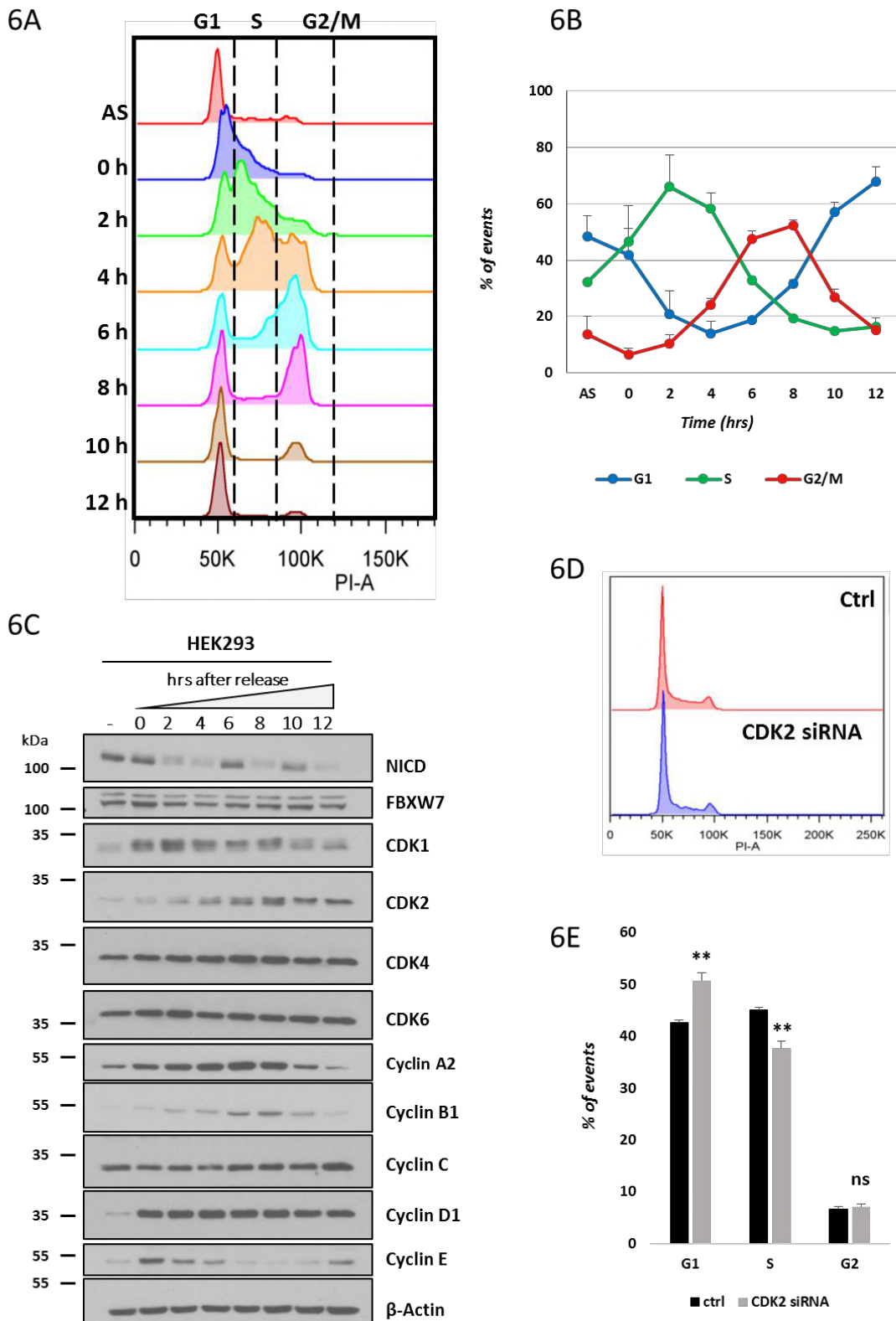
Figure 6. NICD levels fluctuate during the cell cycle. (A) Cell cycle profile for HEK293 cells released from synchronization after double thymidine block. Cells were released and

35

698 harvested at the indicated time points (AS= asynchronous). Analysis of cell cycle arrest and

699 release was performed using propidium iodide (PI) staining and flow cytometry. A

700 representative experiment of three performed is shown.

701 (B) Chart of flow cytometry data shows the percentage of HEK293 cells in G1, S and the G2/M

702 phases after release from double thymidine treatment. Time points are expressed as mean ±

703 SEM from three independent experiments.

704 (C) Expression of the indicated proteins in HEK293 cells was examined by western blotting,

705 and β-Actin was used as loading control. This summary is a representation of three

706 independent experiments.

707 (D) Cell cycle profile for HEK293 cells 48h after transfection with plasmids encoding scrambled

708 siRNA or siRNA specific for CDK2. Analysis of cell cycle arrest and release was performed

709 using propidium iodide (PI) staining and flow cytometry. A representative experiment of three

710 performed is shown.

711 (E) Graph of flow cytometry data shows the percentage of cells in given cell-cycle phases 48h

712 after transfection with plasmids encoding scrambled siRNA or siRNA specific for CDK2. Graph

713 represents the mean of three independent experiments. All data represent the mean ± SEM

714 from three independent experiments. Student's t-test analysis was performed, with **$p \leq 0.01$

715 (ns=not significant).

716 **Figure 7**

717
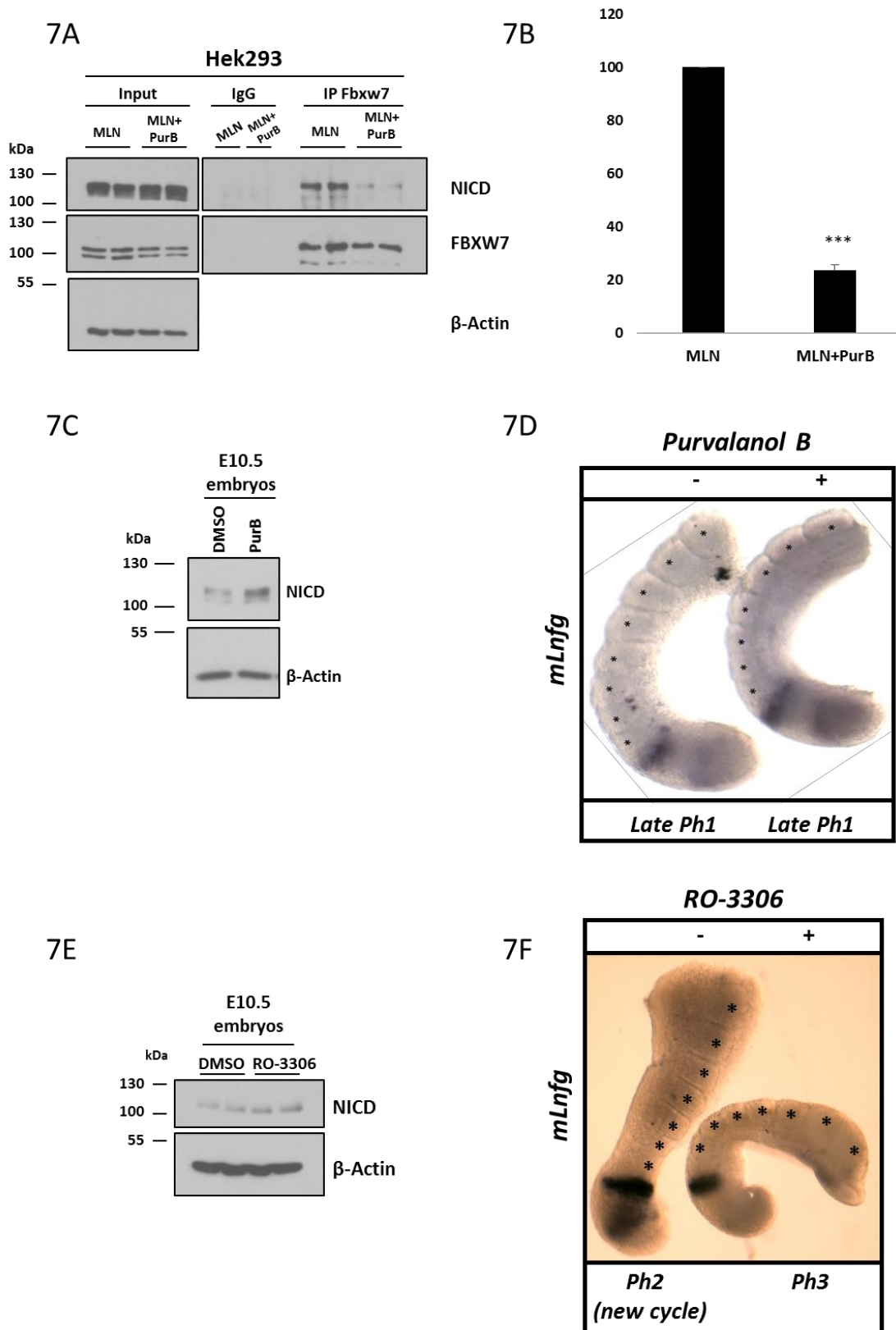
Figure 7. **Purvalanol B treatment reduces NICD-FBXW7 interaction and delays the pace of the segmentation clock in mouse PSM explants**. (A) Purvalanol B treatment reduced the NICD-FBXW7 interaction. 200 µg of HEK293 cell lysates treated with MLN4924 or MLN4924 in combination with 0.1 µM of Purvalanol B were subjected to immunoprecipitation using FBXW7 antibody, or IgG antibody as negative control, and precipitated material was analysed by western blot using NICD antibody. Western blot with FBXW7 antibody served as loading control for immunoprecipitation efficiency. 10% of cell lysate before immunoprecipitation was used as input control and β-Actin has been used as loading control. (B) Quantification of the density of western blot bands in (A) performed by ImageJ software. Data are expressed as fold changes compared to MLN4924 treated samples. All data represent the mean ± SEM from three independent experiments. Student's t-test analysis was performed, with ***p≤0.001.

(C) E10.5 mouse tails were bissected down the midline. One half (+) was cultured for 4 hrs in the presence of Purvalanol B (1 µM). The contralateral half (-) was cultured for 4h in the presence of DMSO. Control or treated explants were pooled and NICD levels were detected by western blot. β-Actin was used as loading control.

(D) Bissected E10.5 mouse PSM explants were cultured in the absence (-) or presence (+) of 1µM of Purvalanol B for 4 hours and then analysed by *in situ* hybridization for *mLfng* mRNA expression. Purvalanol B treated explant has one less somite than the control explant and the treated explant is in the same late phase 1 of the oscillation cycle of dynamic *mLfng* mRNA expression indicating it is a whole cycle delayed compared to the "-" explant.

(E) E10.5 mouse tails were bissected down the midline. One half (+) was cultured for 4 hrs in the presence of RO-3306 (10 µM). The contralateral half (-) was cultured for 4h in the presence of DMSO. Control or treated explants were pooled and NICD levels were detected by western blot. β-Actin has been used as loading control.

(F) Bissected E10.5 mouse PSM explants were cultured in the absence (-) or presence (+) of 10 µM of RO-3306 for 4 hours and then analysed by *in situ* hybridization for *mLfng* mRNA expression. RO-3306 treated explant has one less somite than the control explant and the treated explant is in a phase behind of the oscillation cycle of dynamic *mLfng* mRNA expression indicating there is a delay in the oscillation compared to the "-" explant.

38

748 **Figure 8**
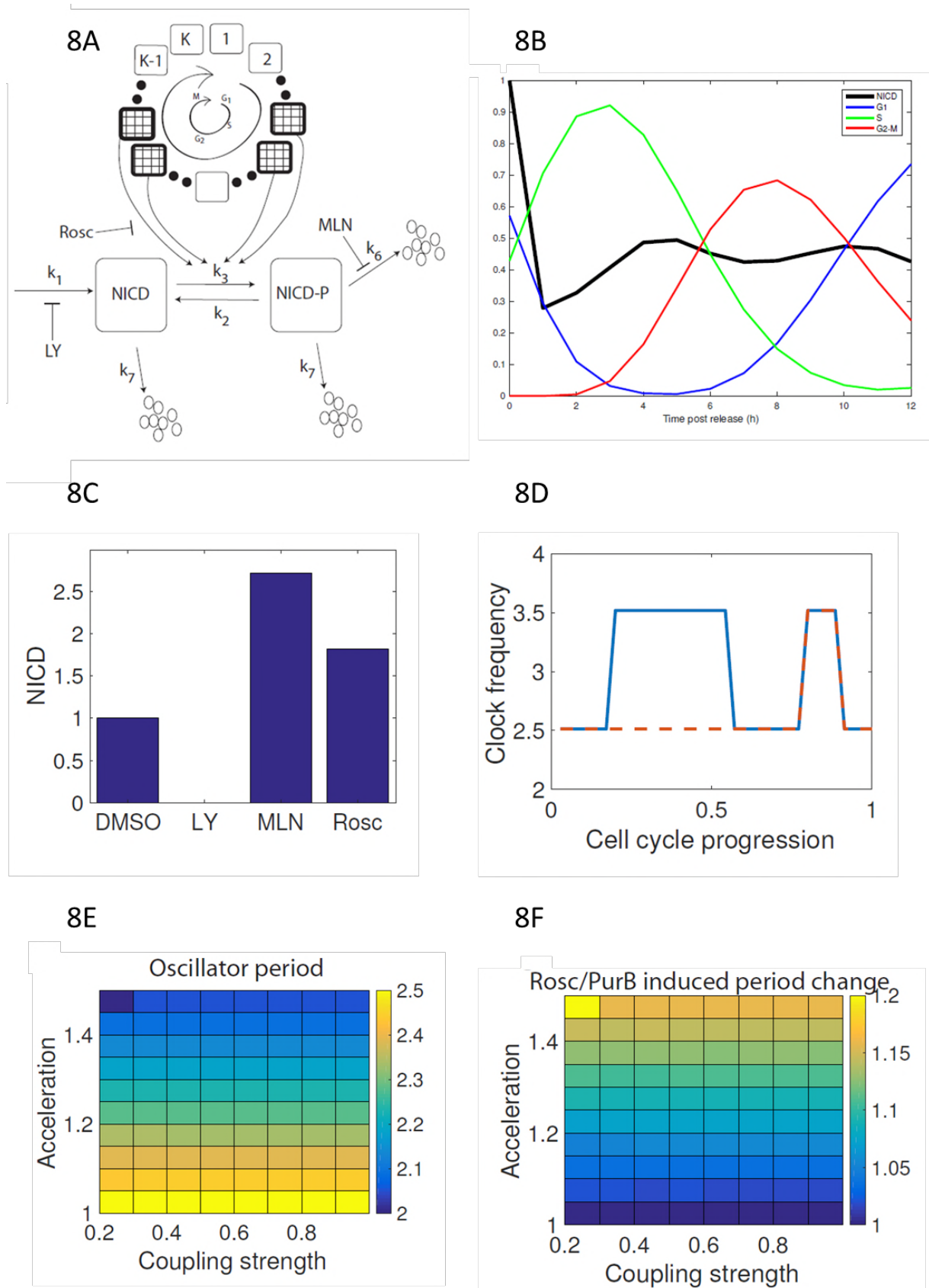
751 **Figure 8. Mathematical model links NICD regulation, segmentation clock and cell cycle.**

752 (A) A schematic illustration of NICD production, phosphorylation and cell-cycle coupled

753 degradation. The cell cycle is represented by clockwise progression through a *K* state model.

754 NICD phosphorylation occurs at two different stages of the cell cycle (patterned boxes). (B)

755 Levels of NICD and cell cycle phase distribution are plotted against time post thymidine

756 release. (C) Steady-state levels of NICD are plotted for simulated control, LY411575,

757 MLN4924 and Purvalanol B/Roscovitine treatments. (D, E, F) Simulating a population of

758 coupled PSM oscillators with cell cycle modulated frequencies. (D) The clock frequency in a

759 single cell is plotted against cell cycle position for normal (solid line) and CDK2 inhibited

760 (dashed line) cells. (E) The emergent population-scale oscillator period is plotted against

761 coupling strength and CDK acceleration factor. (F) Period change (Roscovitine/Purvalanol B

762 versus control) as a result of CDK inhibition is plotted against coupling strength and CDK-

763 mediated acceleration rate.

764 **Supplementary Figure 1**
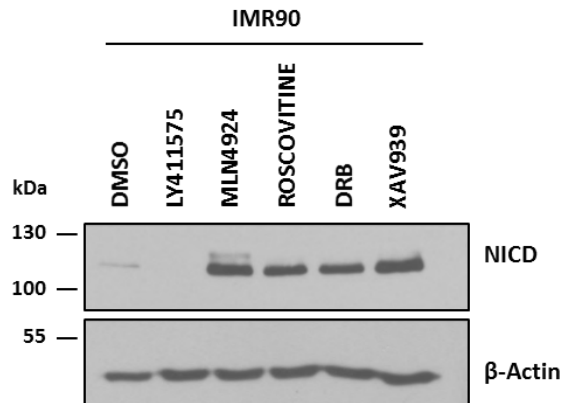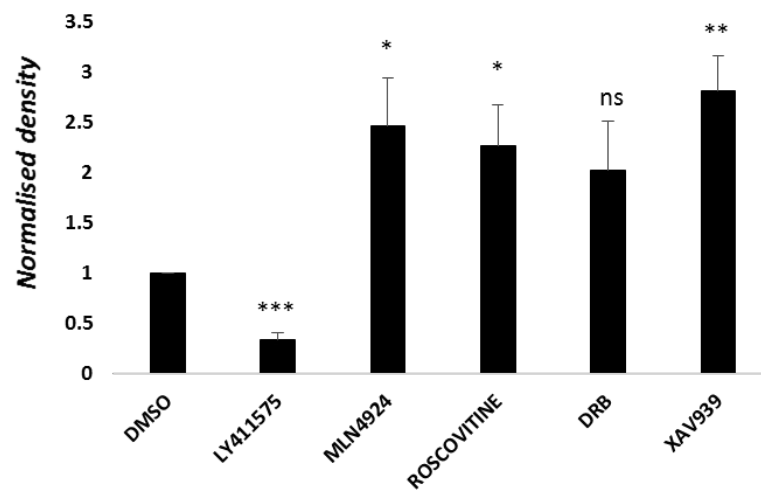
765

766

767 **Supplementary Figure 1**. **Exposure to Roscovitine, DRB or XAV9393 leads to increased**

768 **levels of NICD in IMR90 cells**. (A) IMR90 cells were treated for 3 hours with 150 nM of

769 LY411575, 1 µM of MLN4924, 10 µM of Roscovitine, 10 µM DRB or 10 µM XAV939. DMSO

770 served as vehicle control. Western blot analysis reveals that NICD levels were increased upon

771 treatment with Roscovitine, DRB, XAV939, and MLN4924. NICD is undetectable following

772 LY411575 treatment. β-Actin served as loading control.

773 (B) Quantification of the density of western blot bands in (A) using ImageJ software. Data are

774 expressed as fold changes compared to DMSO. All data represent the mean ± SEM from

775   three independent experiments. Student's t-test analysis was performed, with *p≤0.05,

776   **p≤0.01, and ***p≤0.001.

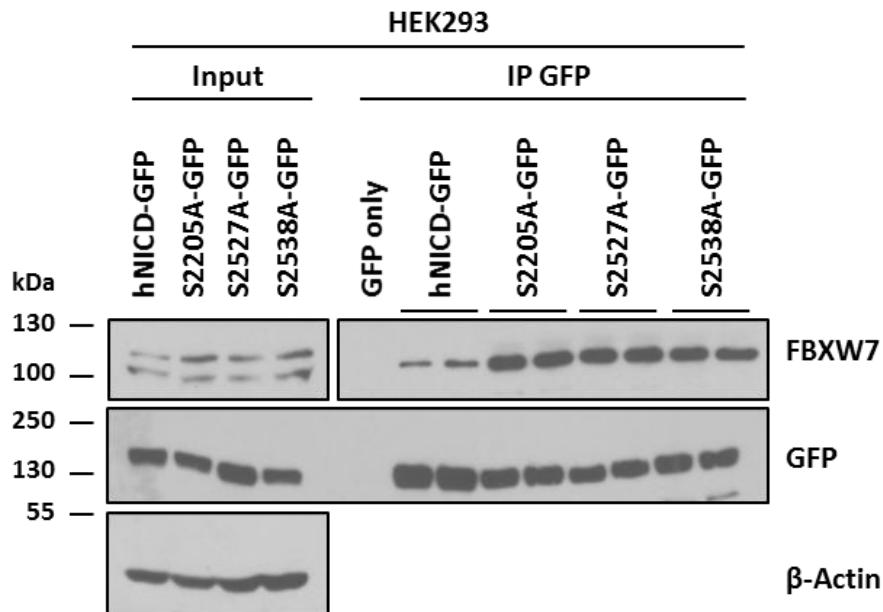777 **Supplementary Figure 2**
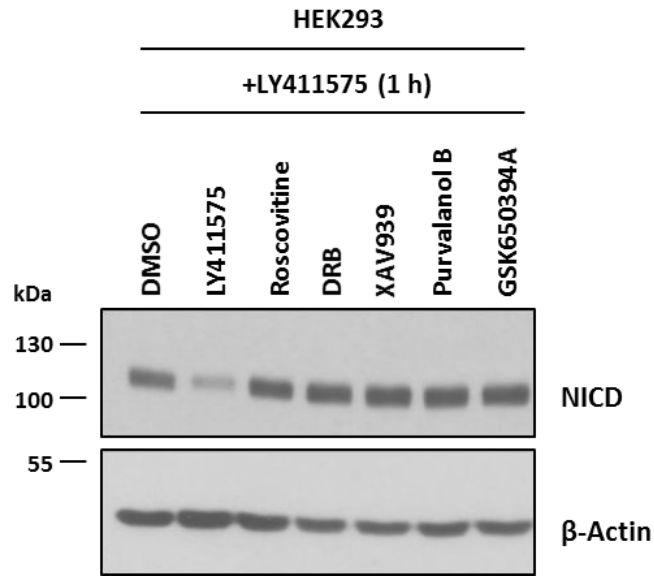
778

779

780 **Supplementary Figure 2**. **Increase in endogenous NICD levels after exposure to small**

781 **molecule inhibitors is due to increased stability, not increased NICD production**.

782 HEK293 cells were treated for 3 hours with 150 nM of LY411575, 10 µM of Roscovitine, 10

783 µM of DRB, 10 µM of XAV939, 0.1 µM of Purvalanol B or 10 µM of GSK650394A. DMSO

784 served as vehicle control. 1 hour prior to lysate collection 150 nM of LY411575 was added to

785 DMSO, Roscovitine, DRB, XAV939, Purvalanol B or GSK650394A treated cells to prevent

786 new NICD production. β-Actin served as loading control.

787   **Supplementary Figure 3**

788
789
790

791   **Supplementary Figure 3**. **Serine to alanine point mutation on NICD Serine 2205, 2527**
792   **and 2538 residues do not change interaction with FBXW7**. hNICD-GFP peptides encoding
793   non-phosphorylatable mutations (serine to alanine) were expressed in HEK293 cells. The
794   exogenously expressed protein was subsequently immunoprecipitated with anti-GFP antibody
795   and precipitated material was analysed by western blot using FBXW7 antibody. Wild-type
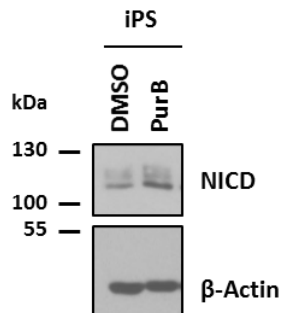796   hNICD-GFP and GFP only vectors were included as positive and negative controls,
797   respectively. Western blot using GFP antibody served as immunoprecipitation efficiency
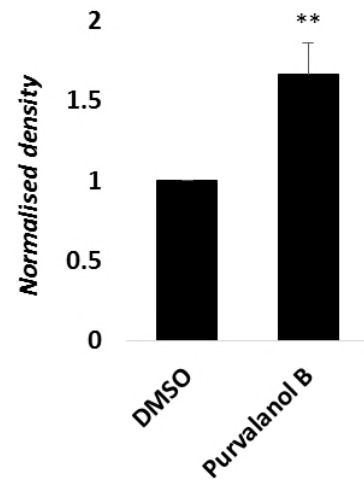798   control. β-Actin has been used as loading control.

44

799 **Supplementary Figure 4**

800

801

802 **Supplementary Figure 4**. **NICD levels increase in iPS cells following treatment with**

803 **Purvalanol B.** (A) iPS cells were treated with 0.1µM of Purvalanol B for 3 hours. Endogenous

804 levels of NICD were detected by western blot. β-Actin has been used as loading control.

805 (B) Quantification of the density of western blot bands in (A) using ImageJ software. Data are

806 expressed as fold changes compared to DMSO. All data represent the mean ± SEM from

807 three independent experiments. Student's t-test analysis was performed, with **p≤0.01.

808 **MATERIALS AND METHODS**

809

810 All plasmids and reagents indicated as such in the text are available from MRC PPU Reagents

811 and Services (https://mrcppureagents.dundee.ac.uk/)

812

813 **Cell Culture**

814 HEK293 (human embryo kidney cells) and IMR90 (Human Caucasian fetal lung fibroblast)

815 cells were obtained from the American Type Culture Collection (ATCC). Cells were routinely

816 cultured and maintained in DMEM High glucose (Gibco) supplemented with 10% Fetal Bovine

817 Serum (FBS; LabTech), 1% Penicillin/Streptomycin (Gibco), 1% Sodium Pyruvate (Gibco) and

818 2mM L-Glutamine (Gibco).

819 ChiPS4 human Induced pluripotent stem (iPS) cells (derived from new born human dermal

820 fibroblasts) were purchased from Cellartis AB and maintained using DEF-CS (Cellartis AB)

821 according to the manufacturer's recommendations. For experiments, cells were seeded as

822 single cells on Geltrex™ coated dishes (10 µg/cm^2) in DEF medium supplemented with 10 µM

823 of Rho-kinase inhibitor Y27632 (Tocris) at a density of 1x54 cells/cm^2 and allowed to attach

824 overnight. The medium was then replaced with fresh DEF medium (Y27632) and after a further

825 24 hrs cells were treated with inhibitors.

826 All cells were grown at 37°C in 5% CO_2.

827 Cells were trypsinized and split into new plates at subconfluency.

828

829 **Transfections**

830 **Overexpression transfections**

831 HEK293 cells were seeded 24 hrs prior to transfection and then transiently transfected

832 following the GeneJuice® Transfection Reagent protocol provided by Merck Millipore.

833 Depending on plate size, 2-9 µg of plasmid was used. Cells were harvested 24 hrs after

834 transfection.

835

836 **siRNA transfections**

837 Small interfering RNA oligonucleotides were purchased from MWG/Eurofins and used in a

838 stock concentration of 20µM. siRNAs were transfected using calcium phosphate transfection

839 method [83]. siRNA oligonucleotides were diluted in a solution containing distilled sterile H_2O

840 and 2M $CaCl_2$.

841 The mixture was then added drop-wise to a round-bottom 15ml tube containing 2X HBS

842 (0.137M NaCl, 0.75M Na2HPO4, 20mM HEPES pH 7.0). The content was then added to cells

843 and incubated overnight at 37°C. Media was changed after 24 hrs and cells were harvested

844 after 48 hrs of transfection.

845

846 **Oligonucleotide Sequences for siRNA Knockdown siRNA**

siRNA	Sequence (5'→3')
Control	AACAGUCGCGUUUGCGACUGG
CDK1	AAGGGGUUCCUAGUACUGCAA
CDK2	CCUCAGAAUCUGCUUAUUA
FBXW7	ACAGGACAGUGUUUACAAA

847

848 Commercial CDK8 siRNA (Cell Signalling, #6438) has been used.

849

850 **Plasmids and mutagenesis**

851 hNICD-GFP vector was generated and obtained from MRC-PPU reagents, University of

852 Dundee. All NOTCH1 mutants were generated and obtained from MRC-PPU reagents,

853 University of Dundee.

854 Briefly, the fragment NOTCH1 1754-2555 (end) was synthesized by GeneArt with flanking

855 BamHI and NotI restriction sites to facilitate cloning, the sequence was codon-optimized for

856 mammalian expression. This was then digested and ligated into expression vector pCMV5D

857 GFP to make the wild type clone pCMV5D GFP NOTCH1 1754-end.

47

858   Site-directed mutagenesis was carried out using the QuikChange Lightning Site-Directed

859   Mutagenesis Kit (Agilent Technologies) but substituting the Taq with KOD Hot Start DNA

860   polymerase (Novagen). All mutations were confirmed by sequencing.

861

862   S2205A change was introduced using primers

863   Forward: 5'-CCCGTGGATAGCCTGGAAGCGCCTCACGGCTACCTGAGC

864   Reverse: 5'-GCTCAGGTAGCCGTGAGGCGCTTCCAGGCTATCCACGGG

865

866   S2513A change was introduced using primers:

867   Forward: 5'-CCCATTTCTGACCCCTGCACCCGAGAGCCCCGATC

868   Reverse: 5'-ATCGGGGCTCTCGGGTGCAGGGGTCAGAAATGGG

869

870   S2516A change was introduced using primers

871   Forward: 5'-CTGACCCCTAGCCCCGAGGCGCCCGATCAGTGGTCTAGC

872   Reverse: 5'-GCTAGACCACTGATCGGGCGCCTCGGGGCTAGGGGTCAG

873

874   S2513A and S2516A double mutant was generated with primers:

875   Forward: 5'-CACCCCTTCCTCACCCCGGCCCCTGAGGCCCCTGACCAGTGGTCCA

876   Reverse: 5'-TGGACCACTGGTCAGGGGCCTCAGGGGCCGGGGTGAGGAAGGGGTG

877

878   S2527A change was introduced using primers

879   Forward: 5'-TCTAGCAGCAGCCCCCACGCGAACGTGTCCGATTGGAGC

880   Reverse: 5'-GCTCCAATCGGACACGTTCGCGTGGGGGCTGCTGCTAGA

881

882   S2538A change was introduced using primers

883   Forward: 5'-TGGAGCGAAGGCGTGTCCGCCCCCCCAACCAGCATGCAG

884   Reverse: 5'-CTGCATGCTGGTTGGGGGGGCGGACACGCCTTCGCTCCA

885

48

Treatments

Cells were treated for 3 hrs with different drugs: 150 nM of LY411575 (generated in house, University of Dundee) [9], 1µM of MLN4924 (MRC-PPU reagents, University of Dundee), 10 µM of 5,6-Dichloro-1-beta-D-ribofuranosylbenzimidazole (DRB) (Sigma), 10 µM of Roscovitine (Calbiochem), 10 µM of XAV939 (Tocris Bioscience), 0.1 µM of Purvalanol B (MRC-PPU reagents, University of Dundee), 10 µM of GSK650394A (MRC-PPU reagents, University of Dundee), 10 µM of RO-3306 (Sigma) and DMSO (Sigma) as control. Lysates were treated with λ-phosphatase (New England BioLabs) following the manufacturer's instructions.

Protein extraction

Cells were lysed on ice for 15 min by adding the appropriate volume of lysis buffer (50mM Tris-HCl pH 7.5, 150mM NaCl, 1mM EDTA, 1mM EGTA, 10mM NaF, 1mM Na3VO4, 0.1% β-mercaptoEtOH, 1 tablet of protease inhibitor cocktail, Thermo Scientific).

Cells were harvested by scraping and the lysate was clarified by centrifugation for 15 min at 14000 rcf at 4°C. The supernatants were collected and stored at -80°C.

Bradford reagent (BioRad) has been used as the colorimetric assay for protein measurements.

Western Blot

20 to 50µg of protein were diluted 1:1 with 2x loading buffer (100mM Tris HCL pH 6.8, 20% glycerol, 4% SDS, 200mM DTT and Bromophenol Blue) and proteins were denatured for 5 mins at 95°C. Samples were resolved on a SDS-PAGE following standard procedures.

Gels were transferred onto Nitrocellulose membrane (GE Healthcare) for 1.5 hrs at 400mA. The membrane was then blocked with 5% Milk in TBS-tween buffer (20mM Tris pH 7.6, 150mM NaCl, 0.1% Tween) for 20 minutes. Membranes were incubated 30 minutes/1 hour or O/N at 4°C in primary antibodies.

Antibodies and dilutions are shown in **Table 2**.

913   The membranes were then washed with TBS-Tween and incubated with the appropriate

914   secondary HRP antibody (Cell Signalling, #7074, #7076). After washing, membranes were

915   developed using ECL solution (Pierce).

916

917   **Table 2.**

Antibody	Species	Dilution	Manufactured
Cleaved Notch1	*Rabbit*	1:1000	Cell Signalling #4147
β-Actin	*Mouse*	1:10000	Proteintech #66009-1-Ig
Fbxw7	*Rabbit*	1:1000	Abcam #171961
GFP	*Mouse*	1:1000	Cell Signalling #2956
Cdk1	*Rabbit*	1:1000	Cell Signalling #9116
Cdk2	*Rabbit*	1:1000	Cell Signalling #2546
Cdk4	*Rabbit*	1:1000	Santa Cruz #260
Cdk6	*Rabbit*	1:1000	Santa Cruz #177
Cdk8	*Rabbit*	1:1000	Bethyl #A302-501A-T
Cyclin A2	*Mouse*	1:1000	Cell Signalling #4656
Cyclin B1	*Rabbit*	1:1000	Cell Signalling #4138
Cyclin C	*Rabbit*	1:1000	Bethyl #A301-989A-M
Cyclin D1	*Rabbit*	1:5000	Abcam #137875
Cyclin E1	*Mouse*	1:1000	Cell Signalling #4129
Total Histone H3	*Rabbit*	1:1000	Cell Signalling #9715
Phospho Histone H3	*Rabbit*	1:1000	Cell Signalling #3377

918

919   **Immunoprecipitation**

920   200ug to 1 mg of proteins were incubated O/N at 4°C on rotation with 2 µg of Fbxw7 antibody

921   (Bethyl, A301-721A). Rabbit IgG was used as negative control. Protein G Agarose beads (Cell

922   Signalling #37478) were added for 2 hrs at 4°C on rotation. Precipitates were washed 3 times

923   with cold PBS before adding 2x loading buffer. Samples were denatured for 5 mins at 95°C

924   and then analysed by Western Blot.

925   Immunoprecipitation using GFP-Trap®_A beads (ChromoTek) was performed according to

926   the manufacturer's instructions.

927

928   **Phos-tag gel**

929   Prior loading into the gels for Phos-tag SDS-PAGE, samples were supplemented with 10 mM

930   MnCl2. Phos-tag SDS-PAGE was carried out as previously described [62, 84]. After

931   electrophoresis, gels were washed three times for 10 min each in the transfer buffer [48 mM

932   Tris/HCl, 39 mM glycine and 20% (v/v) methanol] containing 10 mM EDTA and 0.05% (w/v)

933   SDS, followed by one wash in the transfer buffer containing 0.05% SDS for 10 min. Proteins

934   were transferred and incubated with specific antibodies as previously described.

935

936   **Mass Spectrometry**

937   Upon separation by SDS-PAGE on NuPAGE™ 4-12% Bis-Tris protein gels (Thermo

938   Scientific) and staining with Instant Blue (Expedeon), protein bands were excised from gels.

939   Samples were reduced with 10mM DTT at 50°C for 30 min and alkylated with 100mM IAA at

940   room temperature for 20 min in the dark.

941   Digestion was carried out by adding sequencing grade chymotrypsin (Sigma) at a ratio of 1 to

942   50 (enzyme to substrate) and incubating O/N at 30°C.

943   Peptides were extracted with 100% ACN containing 2.5% formic acid and dried in a vacuum

944   centrifuge.

945   Mass spectrometric analysis was performed by LC-MS-MS using a linear ion trap-orbitrap

946   hybrid mass spectrometer (LTQ-Orbitrap Velos, Thermo Fisher Scientific) and coupled to a

947   Dionex Ultimate 3000 nanoLC system. Peptides were typically injected onto a Thermo

948   Scientific 15cm Easy spray column (Part No. ES800), with a flow of 300 nl/min and eluted over

949   a 40 min linear gradient of 97% solvent A (3% DMSO, 2% Acetonitrile, 0.1% formic acid in

950   H_2O) to 35% solvent B (90% acetonitrile, 3% DMSO, 0.08% formic acid in H_2O). Data files

51

951 were analysed by Proteome Discoverer 2.0 (Thermo), using Mascot 2.4.1

952 (www.matrixscience.com), and searching against the Swissprot and MRC-PPU (University of

953 Dundee) databases. Scaffold (www.ProteomeSoftware.com) was also used to examine the

954 Mascot result files. Allowance was made for the following modifications: fixed,

955 Carbamidomethyl (C), and variable, Oxidation (M), Dioxidation (M) and Phosphorylation (S, T

956 and Y). Error tolerances were 10ppm for MS1 and 0.6 Da for MS2. Phospho-sites were

957 assigned according to Proteome Discoverer ptmRS when the phospho-RS site probability was

958 greater than or equal to 90%.

959

Kinase assay

961 Kinase assay was designed and performed by MRC-PPU International centre for Kinase

962 Profiling at University of Dundee (http://www.kinase-screen.mrc.ac.uk/). All assays were

963 carried out using a radioactive (33P-ATP) filter-binding assay.

964

Fluorescence-Activated Cell Sorter Analysis

966 HEK293 cells were harvested, pelleted by gentle centrifugation (450g x 5 min) and washed

967 once in 1 ml of PBS+1% v/v FBS and transferred to FACS tubes (Scientific Laboratory

968 Supplies).

969 Cells were pelleted again and then fixed in cold 70% ethanol for 30 minutes at room

970 temperature.

971 Cells number was adjusted to approximately 5×10^5 cells and then cells were washed twice in

972 PBS+1% v/v FBS.

973 Cell pellet was then resuspended in 300 µl of staining buffer (50 µg/ml Propidium iodide, 50

974 µg/ml RNase A in PBS+1% v/v FBS) and incubated for 30 min in the dark at room temperature.

975 FACS analyses were conducted by Flow Cytometry and Cell Sorting facility (University of

976 Dundee).

977 Briefly, samples were analyzed on a FACS Canto II flow cytometer from Becton Dickinson.

978 Propidium Iodine was detected using 488nm excitation and emission collected at 587 +/- 40

979   nm. Data were analyzed using Flowjo software (Flowjo, LLC). Single cells were identified on

980   the basis of PI-A and PI-W measurements and doublets excluded. Cell cycle distribution of

981   the resulting PI-A histograms were determined using the Watson-Pragmatic model.

982

983   **Cell cycle synchronization**

984   To synchronize HEK293 cells at G1/S, a double-thymidine block assay was performed. Cells

985   were treated with 2.5 mM of thymidine (Sigma) for 18 hrs, washed twice with PBS, released

986   into fresh media for 9 hrs, treated for a further 14 hrs with 2.5mM of thymidine, then released

987   again into fresh media following two washes in PBS. Cells were then collected for FACS and

988   Western Blot protein analyses at the indicated time points, following protocols already

989   described.

990

991   **Mouse Embryo Explant Culture**

992   E10.5 CD1 mice embryos were harvested and explants were prepared as previously

993   described [85]. Each embryo's posterior part was divided into two halves by cutting along the

994   neural tube. The explants were cultured in hanging drops of culture medium composed of

995   DMEM/F12 (Gibco), 10% FBS, 1% penicillin–streptomycin, 10 ng/ml Fgf2 (PeproTech).

996   One half was cultured in medium containing Purvalanol B (1 µM) or RO-3306 (10 µM),

997   whereas the control side was cultured in normal medium (DMSO). Both sides were cultured

998   for 4 hr and then analysed for expression of *Lfng* mRNA by in situ hybridization.

999   For the Western Blot analysis PSM explants from 5 embryos were cultured in DMSO control

1000 vehicle and the corresponding contralateral 5 PSM explants cultured in the presence of a small

1001 molecule inhibitor.

1002 Experiments were conducted in strict adherence to the Animals (Scientific Procedures) Act of

1003 1986 and UK Home Office Codes of Practice for use of animals in scientific procedures.

1004

1005 **In situ hybridisation of PSM explants using exonic RNA probes**

1006   For whole-mount embryos and explants, in situ hybridisation analysis was performed with the

1007   use of exonic anti-sense RNA probes as previously described [86].

1008   Samples were imaged using a Leica bright field dissection microscope using Volocity

1009   acquisition software. The number of somites present in each explant (identical between

1010   explant pairs but variable between embryos) was recorded.

1011   To fix the tissue, samples were incubated for 2 hrs at RT in 4 % PFA/PBS, washed copiously

1012   in PBST and transferred into sealed Eppendorf tubes containing 0.01 % sodium azide/PBS

1013   for long-term storage at 4°C.

1014

1015   **Statistical Analysis**

1016   Unless indicated, Statistical analyses were performed using GraphPad software.

1017   Student t-tests were performed in all the data comparing control to treatment conditions, with

1018   P values calculated as * p≤0.05, **p≤0.01 and ***p≤0.001. All experiments have been

1019   performed at least three times.

ACKNOWLEDGEMENTS

We would like to thank Ioanna Mastromina and Michaela Omelkova for reading of the manuscript and constructive feedbacks. Special thanks also go to Genta Ito for assistance with Phostag gel assay. We thank the groups of D. Alessi and S. Rocha for reagents and Laura D'Ignazio for experimental assistance. The authors would like to thank Rachel Toth, Mel Wightman and Tom Macartney (MRC-PPU Reagents and Services) for cloning and Dr David Campbell, Bob Gourlay and Joby Vhargese (MRC-PPU) for Mass Spectrometry analysis. We also thank Professor Daan van Aalten, Professor Victoria Cowling, Dr Francesca Tonelli and Dr Houjiang Zhou for their input.

COMPETING INTERESTS

I can confirm there are no competing interests for any of the named authors.

55

REFERENCES

1. Maroto, M., R.A. Bone, and J.K. Dale, *Somitogenesis.* Development, 2012. **139**(14): p. 2453-2456.

2. Gomez, C. and O. Pourquie, *Developmental control of segment numbers in vertebrates.* J Exp Zool B Mol Dev Evol, 2009. **312**(6): p. 533-44.

3. Hubaud, A. and O. Pourquie, *Signalling dynamics in vertebrate segmentation.* Nat Rev Mol Cell Biol, 2014. **15**(11): p. 709-21.

4. Gossler, A. and M. Hrabe de Angelis, *Somitogenesis.* Curr Top Dev Biol, 1998. **38**: p. 225-87.

5. Dequeant, M.L., et al., *A complex oscillating network of signaling genes underlies the mouse segmentation clock.* Science, 2006. **314**(5805): p. 1595-8.

6. Gibb, S., M. Maroto, and J.K. Dale, *The segmentation clock mechanism moves up a notch.* Trends Cell Biol, 2010. **20**(10): p. 593-600.

7. Pourquie, O., *Vertebrate segmentation: from cyclic gene networks to scoliosis.* Cell, 2011. **145**(5): p. 650-63.

8. Sparrow, D.B., et al., *A mechanism for gene-environment interaction in the etiology of congenital scoliosis.* Cell, 2012. **149**(2): p. 295-306.

9. Ferjentsik, Z., et al., *Notch is a critical component of the mouse somitogenesis oscillator and is essential for the formation of the somites.* PLoS Genet, 2009. **5**(9): p. e1000662.

10. Jiang, Y.J., et al., *Notch signalling and the synchronization of the somite segmentation clock.* Nature, 2000. **408**(6811): p. 475-9.

11. Hubaud, A., et al., *Excitable Dynamics and Yap-Dependent Mechanical Cues Drive the Segmentation Clock.* Cell, 2017. **171**(3): p. 668-682 e11.

12. Delaune, E.A., et al., *Single-cell-resolution imaging of the impact of Notch signaling and mitosis on segmentation clock dynamics.* Dev Cell, 2012. **23**(5): p. 995-1005.

13. Liao, B.K. and A.C. Oates, *Delta-Notch signalling in segmentation.* Arthropod Struct Dev, 2017. **46**(3): p. 429-447.

14. Lewis, J., *Autoinhibition with transcriptional delay: a simple mechanism for the zebrafish somitogenesis oscillator.* Curr Biol, 2003. **13**(16): p. 1398-408.

15. Monk, N.A., *Oscillatory expression of Hes1, p53, and NF-kappaB driven by transcriptional time delays.* Curr Biol, 2003. **13**(16): p. 1409-13.

16. Ay, A., et al., *Short-lived Her proteins drive robust synchronized oscillations in the zebrafish segmentation clock.* Development, 2013. **140**(15): p. 3244-53.

17. Hanisch, A., et al., *The elongation rate of RNA polymerase II in zebrafish and its significance in the somite segmentation clock.* Development, 2013. **140**(2): p. 444-53.

18. Wiedermann, G., et al., *A balance of positive and negative regulators determines the pace of the segmentation clock.* Elife, 2015. **4**: p. e05842.

19. Harima, Y., et al., *Accelerating the tempo of the segmentation clock by reducing the number of introns in the Hes7 gene.* Cell Rep, 2013. **3**(1): p. 1-7.

20. Liao, B.K., D.J. Jorg, and A.C. Oates, *Faster embryonic segmentation through elevated Delta-Notch signalling.* Nat Commun, 2016. **7**: p. 11861.

21. Schroter, C. and A.C. Oates, *Segment number and axial identity in a segmentation clock period mutant.* Curr Biol, 2010. **20**(14): p. 1254-8.

22. Herrgen, L., et al., *Intercellular coupling regulates the period of the segmentation clock.* Curr Biol, 2010. **20**(14): p. 1244-53.

23. Kim, W., et al., *The period of the somite segmentation clock is sensitive to Notch activity.* Mol Biol Cell, 2011. **22**(18): p. 3541-9.

24. Nowell, C.S. and F. Radtke, *Notch as a tumour suppressor.* Nature Reviews Cancer, 2017. **17**(3): p. 145-159.

25. Koch, U., R. Lehal, and F. Radtke, *Stem cells living with a Notch.* Development, 2013. **140**(4): p. 689-704.

26. Lai, E.C., *Notch signaling: control of cell communication and cell fate.* Development, 2004. **131**(5): p. 965-73.

27. Artavanis-Tsakonas, S., M.D. Rand, and R.J. Lake, *Notch signaling: cell fate control and signal integration in development.* Science, 1999. **284**(5415): p. 770-6.

28. Penton, A.L., L.D. Leonard, and N.B. Spinner, *Notch signaling in human development and disease.* Semin Cell Dev Biol, 2012. **23**(4): p. 450-7.

29. Lowell, S., et al., *Notch promotes neural lineage entry by pluripotent embryonic stem cells.* PLoS Biol, 2006. **4**(5): p. e121.

30. Kopan, R. and M.X. Ilagan, *The canonical Notch signaling pathway: unfolding the activation mechanism.* Cell, 2009. **137**(2): p. 216-33.

31. Kovall, R.A., et al., *The Canonical Notch Signaling Pathway: Structural and Biochemical Insights into Shape, Sugar, and Force.* Dev Cell, 2017. **41**(3): p. 228-241.

32. Carrieri, F.A. and J.K. Dale, *Turn It Down a Notch.* Front Cell Dev Biol, 2016. **4**: p. 151.

33. Kovall, R.A., et al., *The Canonical Notch Signaling Pathway: Structural and Biochemical Insights into Shape, Sugar, and Force.* Developmental Cell, 2017. **41**(3): p. 228-241.

34. Espinosa, L., et al., *Phosphorylation by glycogen synthase kinase-3 beta down-regulates Notch activity, a link for Notch and Wnt pathways.* J Biol Chem, 2003. **278**(34): p. 32227-35.

35. Fryer, C.J., J.B. White, and K.A. Jones, *Mastermind recruits CycC:CDK8 to phosphorylate the Notch ICD and coordinate activation with turnover.* Mol Cell, 2004. **16**(4): p. 509-20.

36. Jin, Y.H., et al., *Regulation of Notch1/NICD and Hes1 expressions by GSK-3alpha/beta.* Mol Cells, 2009. **27**(1): p. 15-9.

37. O'Neil, J., et al., *FBW7 mutations in leukemic cells mediate NOTCH pathway activation and resistance to γ-secretase inhibitors.* The Journal of Experimental Medicine, 2007. **204**(8): p. 1813-1824.

38. Nowell, C. and F. Radtke, *Cutaneous Notch signaling in health and disease.* Cold Spring Harb Perspect Med, 2013. **3**(12): p. a017772.

39. Roy, M., W.S. Pear, and J.C. Aster, *The multifaceted role of Notch in cancer.* Curr Opin Genet Dev, 2007. **17**(1): p. 52-9.

40. Weng, A.P., et al., *Activating mutations of NOTCH1 in human T cell acute lymphoblastic leukemia.* Science, 2004. **306**(5694): p. 269-71.

41. Wang, K., et al., *PEST domain mutations in Notch receptors comprise an oncogenic driver segment in triple-negative breast cancer sensitive to a gamma-secretase inhibitor.* Clin Cancer Res, 2015. **21**(6): p. 1487-96.

42. Bolos, V., et al., *Notch activation stimulates migration of breast cancer cells and promotes tumor growth.* Breast Cancer Res, 2013. **15**(4): p. R54.

43. Crusio, K.M., et al., *The ubiquitous nature of cancer: the role of the SCF(Fbw7) complex in development and transformation.* Oncogene, 2010. **29**(35): p. 4865-73.

44. O'Neil, J., et al., *FBW7 mutations in leukemic cells mediate NOTCH pathway activation and resistance to gamma-secretase inhibitors.* J Exp Med, 2007. **204**(8): p. 1813-24.

45. Davis, R.J., M. Welcker, and B.E. Clurman, *Tumor suppression by the Fbw7 ubiquitin ligase: mechanisms and opportunities.* Cancer Cell, 2014. **26**(4): p. 455-64.

46. Wu, G., et al., *SEL-10 is an inhibitor of notch signaling that targets notch for ubiquitin-mediated protein degradation.* Mol Cell Biol, 2001. **21**(21): p. 7403-15.

47. Oberg, C., et al., *The Notch intracellular domain is ubiquitinated and negatively regulated by the mammalian Sel-10 homolog.* J Biol Chem, 2001. **276**(38): p. 35847-53.

48. Gupta-Rossi, N., et al., *Functional interaction between SEL-10, an F-box protein, and the nuclear form of activated Notch1 receptor.* J Biol Chem, 2001. **276**(37): p. 34371-8.

49. Skaar, J.R., J.K. Pagan, and M. Pagano, *Mechanisms and function of substrate recruitment by F-box proteins.* Nat Rev Mol Cell Biol, 2013. **14**(6): p. 369-81.

50. Hao, B., et al., *Structure of a Fbw7-Skp1-cyclin E complex: multisite-phosphorylated substrate recognition by SCF ubiquitin ligases.* Mol Cell, 2007. **26**(1): p. 131-43.

1140   51.   Wagner, S.A., et al., *Proteomic analyses reveal divergent ubiquitylation site patterns*
1141   *in murine tissues.* Mol Cell Proteomics, 2012. **11**(12): p. 1578-85.
1142   52.   Kim, W., et al., *Systematic and quantitative assessment of the ubiquitin-modified*
1143   *proteome.* Mol Cell, 2011. **44**(2): p. 325-40.
1144   53.   Moretti, J. and C. Brou, *Ubiquitinations in the notch signaling pathway.* Int J Mol Sci,
1145   2013. **14**(3): p. 6359-81.
1146   54.   Cicenas, J., et al., *Roscovitine in cancer and other diseases.* Annals of Translational
1147   Medicine, 2015. **3**(10).
1148   55.   MacCallum, D.E., et al., *Seliciclib (CYC202, R-Roscovitine) induces cell death in*
1149   *multiple myeloma cells by inhibition of RNA polymerase II-dependent transcription and*
1150   *down-regulation of Mcl-1.* Cancer Res, 2005. **65**(12): p. 5399-407.
1151   56.   Yankulov, K., et al., *The transcriptional elongation inhibitor 5,6-dichloro-1-beta-D-*
1152   *ribofuranosylbenzimidazole inhibits transcription factor IIH-associated protein kinase.*
1153   J Biol Chem, 1995. **270**(41): p. 23922-5.
1154   57.   Turinetto, V., et al., *The cyclin-dependent kinase inhibitor 5, 6-dichloro-1-beta-D-*
1155   *ribofuranosylbenzimidazole induces nongenotoxic, DNA replication-independent*
1156   *apoptosis of normal and leukemic cells, regardless of their p53 status.* BMC Cancer,
1157   2009. **9**: p. 281.
1158   58.   Huang, S.-M.A., et al., *Tankyrase inhibition stabilizes axin and antagonizes Wnt*
1159   *signalling.* Nature, 2009. **461**: p. 614.
1160   59.   Luistro, L., et al., *Preclinical Profile of a Potent γ-Secretase Inhibitor Targeting Notch*
1161   *Signaling with In vivo Efficacy and Pharmacodynamic Properties.* Cancer
1162   Research, 2009. **69**(19): p. 7672-7680.
1163   60.   Lanz, T.A., et al., *Studies of Abeta pharmacodynamics in the brain, cerebrospinal fluid,*
1164   *and plasma in young (plaque-free) Tg2576 mice using the gamma-secretase inhibitor*
1165   *N2-[(2S)-2-(3,5-difluorophenyl)-2-hydroxyethanoyl]-N1-[(7S)-5-methyl-6-oxo-6,7-di*
1166   *hydro-5H-dibenzo[b,d]azepin-7-yl]-L-alaninamide (LY-411575).* J Pharmacol Exp
1167   Ther, 2004. **309**(1): p. 49-55.
1168   61.   Nawrocki, S.T., et al., *MLN4924: a novel first-in-class inhibitor of NEDD8-activating*
1169   *enzyme for cancer therapy.* Expert Opin Investig Drugs, 2012. **21**(10): p. 1563-73.
1170   62.   Kinoshita, E., et al., *Phosphate-binding tag, a new tool to visualize phosphorylated*
1171   *proteins.* Mol Cell Proteomics, 2006. **5**(4): p. 749-57.
1172   63.   Gupta-Rossi, N., et al., *Functional interaction between SEL-10, an F-box protein, and*
1173   *the nuclear form of activated Notch1 receptor.* Journal of Biological Chemistry, 2001.
1174   **276**(37): p. 34371-34378.
1175   64.   Oberg, C., et al., *The Notch intracellular domain is ubiquitinated and negatively*
1176   *regulated by the mammalian sel-10 homolog.* Journal of Biological Chemistry, 2001.
1177   **276**(38): p. 35847-35853.
1178   65.   Li, N., et al., *Cyclin C is a haploinsufficient tumour suppressor.* Nat Cell Biol, 2014.
1179   **16**(11): p. 1080-91.
1180   66.   Thompson, B.J., et al., *The SCFFBW7 ubiquitin ligase complex as a tumor suppressor*
1181   *in T cell leukemia.* J Exp Med, 2007. **204**(8): p. 1825-35.
1182   67.   Orlicky, S., et al., *Structural Basis for Phosphodependent Substrate Selection and*
1183   *Orientation by the SCFCdc4 Ubiquitin Ligase.* Cell, 2003. **112**(2): p. 243-256.
1184   68.   Vassilev, L.T., et al., *Selective small-molecule inhibitor reveals critical mitotic functions*
1185   *of human CDK1.* Proc Natl Acad Sci U S A, 2006. **103**(28): p. 10660-5.
1186   69.   Bashir, T. and M. Pagano, *Cdk1: the dominant sibling of Cdk2.* Nat Cell Biol, 2005.
1187   **7**(8): p. 779-81.
1188   70.   Satyanarayana, A. and P. Kaldis, *Mammalian cell-cycle regulation: several Cdks,*
1189   *numerous cyclins and diverse compensatory mechanisms.* Oncogene, 2009. **28**: p.
1190   2925.
1191   71.   Kassardjian, A., et al., *The Transcription Factor YY1 Is a Novel Substrate for Aurora B*
1192   *Kinase at G2/M Transition of the Cell Cycle.* Vol. 7. 2012. e50645.
1193   72.   Swaffer, M.P., et al., *CDK Substrate Phosphorylation and Ordering the Cell Cycle.* Cell,
1194   2016. **167**(7): p. 1750-1761 e16.

73. Lim, S. and P. Kaldis, *Cdks, cyclins and CKIs: roles beyond cell cycle regulation.* Development, 2013. **140**(15): p. 3079-93.
74. Berthet, C., et al., *Cdk2 knockout mice are viable.* Curr Biol, 2003. **13**(20): p. 1775-85.
75. Chi, Y., et al., *Identification of CDK2 substrates in human cell lysates.* Genome Biol, 2008. **9**(10): p. R149.
76. Santamaria, D., et al., *Cdk1 is sufficient to drive the mammalian cell cycle.* Nature, 2007. **448**(7155): p. 811-U8.
77. Satyanarayana, A., et al., *Genetic substitution of Cdk1 by Cdk2 leads to embryonic lethality and loss of meiotic function of Cdk2.* Development, 2008. **135**(20): p. 3389-400.
78. Diril, M.K., et al., *Cyclin-dependent kinase 1 (Cdk1) is essential for cell division and suppression of DNA re-replication but not for liver regeneration.* Proc Natl Acad Sci U S A, 2012. **109**(10): p. 3826-31.
79. Chiang, M.Y., et al., *Identification of a conserved negative regulatory sequence that influences the leukemogenic activity of NOTCH1.* Molecular and Cellular Biology, 2006. **26**(16): p. 6261-6271.
80. Noseda, M., et al., *Notch activation induces endothelial cell cycle arrest and participates in contact inhibition: role of p21Cip1 repression.* Mol Cell Biol, 2004. **24**(20): p. 8813-22.
81. Joshi, I., et al., *Notch signaling mediates G1/S cell-cycle progression in T cells via cyclin D3 and its dependent kinases.* Blood, 2009. **113**(8): p. 1689-98.
82. Sarmento, L.M., et al., *Notch1 modulates timing of G1-S progression by inducing SKP2 transcription and p27 Kip1 degradation.* J Exp Med, 2005. **202**(1): p. 157-68.
83. Kwon, M. and B.L. Firestein, *DNA transfection: calcium phosphate method.* Methods Mol Biol, 2013. **1018**: p. 107-10.
84. Ito, G., et al., *Phos-tag analysis of Rab10 phosphorylation by LRRK2: a powerful assay for assessing kinase function and inhibitors.* Biochem J, 2016. **473**(17): p. 2671-85.
85. Dale, J.K., et al., *Oscillations of the snail genes in the presomitic mesoderm coordinate segmental patterning and morphogenesis in vertebrate somitogenesis.* Dev Cell, 2006. **10**(3): p. 355-66.
86. Gibb, S., et al., *Interfering with Wnt signalling alters the periodicity of the segmentation clock.* Dev Biol, 2009. **330**(1): p. 21-31.

Mathematical model

1 NICD - Cell cycle model

To account for the experimental observations of NICD degradation in cell lines, we develop a cell cycle dependent model of NICD production and degradation (see Figure 8A). The position of the jth cell in the cell cycle is represented by a set of K discrete state variables, $X_{ij}(t)$, defined such that

$$\sum_{i=1}^{K} X_{ij} = 1, \qquad X_{ij} \in \{0, 1\}. \tag{1}$$

It is assumed that cells transition sequentially between states at rate r_1 and that mitosis is followed by G_1 entry.

The averaged fraction of cells in state i, given by

$$\langle X_i \rangle = \frac{1}{n} \sum_j X_{ij}, \tag{2}$$

where n is the number of cells in the experiment, satisfy

$$\frac{d\langle X_1 \rangle}{dt} = r_1(\langle X_K \rangle - \langle X_1 \rangle), \tag{3}$$

$$\frac{d\langle X_j \rangle}{dt} = r_1(\langle X_{j-1} \rangle - \langle X_j \rangle), \quad j = 2.., K. \tag{4}$$

We note that (author?) (1) propose a similar model and show that relatively large number of compartments ($K = 25$) compartments can be needed to reproduce experimentally observed variances in cell cycle distribution times.

Letting $\langle X(t) \rangle$ represent the population average fraction of cells where CDKs are active, then

$$\langle X \rangle(t) = \sum_{j \in M} \langle X_j \rangle, \tag{5}$$

where M, the set of CDK active states, has m members.

We make the following assumptions about NICD: (i) NICD exists in two states (non-phosphorylated and phosphorylated); (ii) NICD is produced and degraded at constant rates k_1 and k_7, respectively; (iii) NICD is phosphorylated by CDK1 and/or CDK2 at

1

rate k_3; (iv) phosphorylated NICD has a larger degradation rate, k_6, than the background rate, k_7; and (v) dephosphorylation occurs at rate k_2. Letting $N_{1j}(t)$ and $N_{2j}(t)$ represent the amount of NICD and phospho-NICD in the jth cell at time t, the population averages are defined to be

$$\langle N_1 \rangle = \frac{1}{n} \sum_j N_{1j} \quad \text{and} \quad \langle N_2 \rangle = \frac{1}{n} \sum_j N_{2j}, \tag{6}$$

and satisfy

$$\frac{d\langle N_1 \rangle}{dt} = k_1 + k_2 \langle N_2 \rangle - k_3 \langle \sum_{j \in C} X_j N_1 \rangle - k_7 \langle N_1 \rangle, \tag{7}$$

$$\frac{d\langle N_2 \rangle}{dt} = k_3 \langle \sum_{j \in C} X_j N_1 \rangle - k_2 \langle N_2 \rangle - (k_6 + k_7) \langle N_2 \rangle. \tag{8}$$

As the cell cycle variables are uncoupled from the NICD dynamics, in a typical cell line experiment each of the X_j's will tend to the equilibrium value

$$X_j = \frac{1}{K}, \tag{9}$$

and the fraction of CDK active cells is

$$X = \frac{m}{K}.$$

Hence equations (8) reduce to

$$\frac{d\langle N_1 \rangle}{dt} = k_1 + k_2 \langle N_2 \rangle - k_3 \frac{m}{K} \langle N_1 \rangle - k_7 \langle N_1 \rangle, \tag{10}$$

$$\frac{d\langle N_2 \rangle}{dt} = k_3 \frac{m}{K} \langle N_1 \rangle - k_2 \langle N_2 \rangle - (k_6 + k_7) \langle N_2 \rangle. \tag{11}$$

To compute NICD levels equations (11) are solved to steady state (N_1^*, N_2^*) and the total amount of NICD (Figure 8B and 8C) is

$$N^* = N_1^* + N_2^*.$$

LY treatment experiments, in which the production of NICD is reduced owing to gamma-secretase inhibition, are simulated by setting $k_1 = 0$. As PurB/Roscovitine is assumed to inhibit CDK2, the effect in the cell cycle synchronised experiments is to reduce the parameter m. As MLN treatment inhibits FBXW7 mediated degradation, it is simulated by removing the fast decay mode (i.e. $k_6 = 0$).

Now consider a situation in which cells are synchronised as a result of double thymidine block. At the point of release the cell cycle distribution is no longer at equilibrium, rather the initial conditions are

$$X_i(0) = \begin{cases} 1/s & i \in S \\ 0 & \text{otherwise.} \end{cases} \tag{12}$$

where S is a set of states where cells get paused as a result of double thymidine block. After the cells are released from the cell cycle block there are peaks of CDK activity (see Figure 8B) and therefore dynamic levels of NICD.

2 Somitogenesis clock and the cell cycle

To explore the coupling between cell cycle mediated NICD degradation and the somitogenesis clock oscillator in PSM tissue, we introduce an additional set of variables, $\theta_i(t)$, that represent the position of the ith cell in the somitogenesis clock cycle.

As PSM oscillators are coupled via Delta-Notch signalling we consider a phase coupled oscillator model (e.g. 2; 3; 4) of the caudal PSM given

$$\frac{d\theta_i}{dt} = \omega_i(X_1, X_2, .., X_K) + A \sum_j \sin(\theta_j - \theta_i), \tag{13}$$

where ω_i, the natural frequency of the ith cell, is a functional of cell cycle position, the sum is taken over all oscillators and the coupling function represents the effect of Delta-Notch signalling in the caudal PSM.

In a previous model (5) we demonstrated how competition between NICD and Hes7 could yield a phenotype in which increased levels of NICD are correlated with a longer clock period; here we impose this assumption in the phase coupled oscillator model by assuming that the clock frequency is inversely correlated with levels of NICD (Figure 8E). Hence as the cell progresses through the cell cycle, basal levels of NICD fluctuate and modify the natural frequency. We assume that

$$\omega_i(X_1, X_2, ..., X_K) = \begin{cases} r\omega_0 & \text{CDK active} \\ \omega_0 & \text{otherwise.} \end{cases} \tag{14}$$

where the parameter r represents the degree of acceleration of the clock when CDK is active.

Equations (13) –(14) represent a mathematical model of coupled PSM oscillators whose frequencies are modulated by the cell cycle position. The model allows us to explore whether there is an emergent population-scale period and how it is affected by perturbing the cell cycle. To do this we simulate a population of N cells and find that given adequate oscillator coupling the oscillators synchronise to an emergent frequency which is an average over the individual oscillator frequencies

3 Parameter inference

3.1 Cell cycle

The parameters used in the model are presented in Table 2. To recapitulate the cell cycle phase distributions presented in Figure 6 of the Main text we use a 35 state model. The transition rate between compartments, r_1, is defined such that the mean time for a cell to progress from state 1 to is the cell cycle period, $T_C = 12$h. Based upon the data in Figure 6 in the Main Text we assume the cell cycle times presented in Table 2 (see Figure 1).
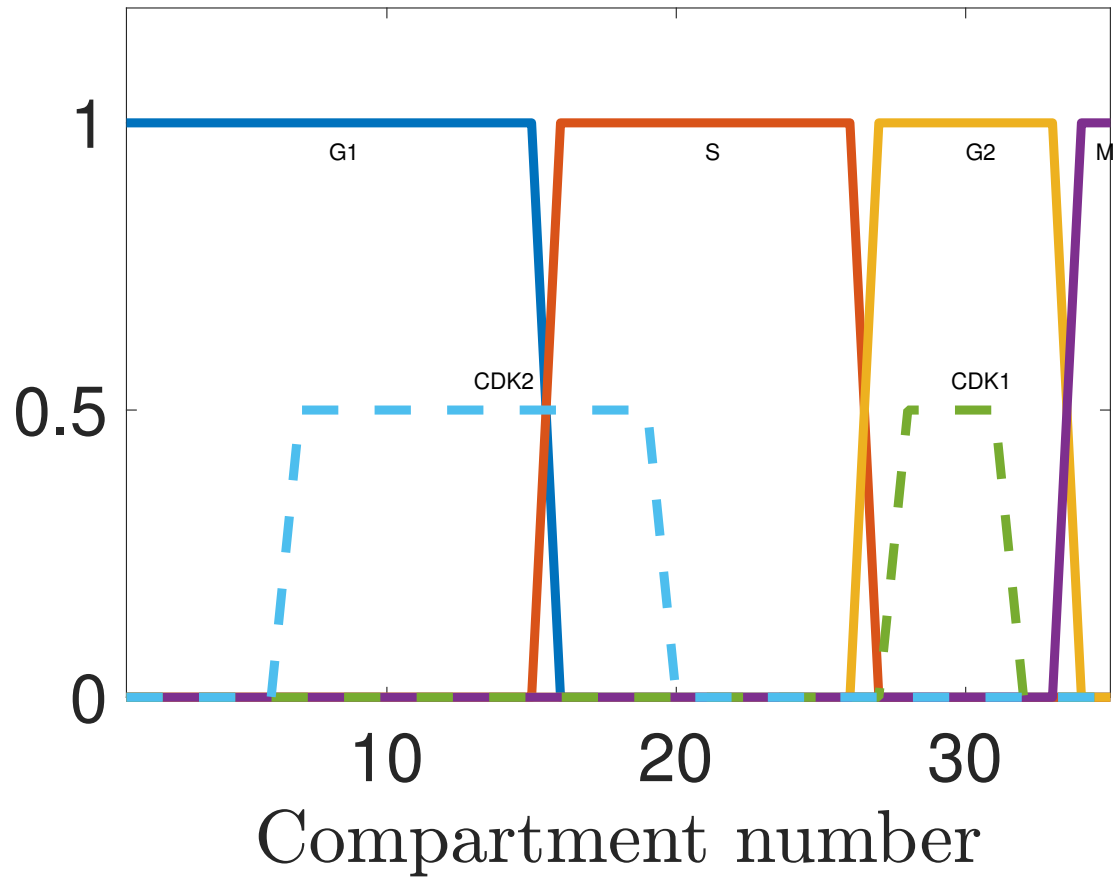
Figure 1: Transition through the cell cycle states (solid lines) and correspondent regions of high CDK2 and CDK 1 activity (dashed lines).

Experiment	NICD	pNICD
Control	0.9	0.1
MLN	1.5	2.0
Rosc	1.3	0.4

Table 1: Quantification of Western blots used for inference of parameters k_2 and k_3.

Parameter	Value	Unit	Description
K	35		Number of compartments in cell cycle model
T_C	12.0	h	Cell cycle period
r_1	$\frac{\ln(2)}{KT_C}$	h^{-1}	Transfer rate between cell cycle states
k_1	10.0	h^{-1}	Rate of NICD production
k_6	12.0	h^{-1}	Fbxw7 mediated NICD degradation rate
k_7	1.6	h^{-1}	Background NICD degradation rate
k_2	3.1	h^{-1}	NICD dephosphorylation rate
k_3	10.0	h^{-1}	NICD phosphorylation rate
ω_0	2.5	h^{-1}	somitogenesis clock frequency
A	[0,2.0]	h^{-1}	Oscillator coupling strength
r	[1,1.5]	h^{-1}	Somitogenesis clock acceleration factor
T_{G_1}	4	h	G1 duration
T_S	3	h	S duration
T_{G_2}	2	h	G2 duration
T_M	1	h	M duration
$CDK2_{on}$	[0.2,0.55]	Nondim	CDK2 active
$CDK1_{on}$	[0.8,0.9]	Nondim	CDK1 active
S	[0.4, 0.75]	Nondim	Thymidine block

Table 2: A table with parameter values.

3.2   NICD modelling

The parameter k_1 represents the number of molecules produced per cell per hour. The fast and slow degradation rates are values inferred from (author?) (5). To determine the parameters k_2 and k_3 we use the DMSO and MLN treatment Blot data presented in Figure 1 of the Main Text. The measured normalised levels of of non-phosphorylated and phosphorylated forms of NICD in different conditions are given in Table 1. A least squares minimisation algorithm is used to minimise the error between the model and the data in Table 1 for the control and MLN datasets. Hence values for the parameters k_2 and k_3 are inferred.

3.3   Somitogenesis clock

The somitogenesis clock period in the mouse PSM is approximately two hours. As we do not have direct measurements of coupling strength or acceleration factor we simulate model behaviour over a range the specified parameter ranges.

References

[1] Yates CA, Ford MJ, Mort RL. A multi-stage representation of cell proliferation as a Markov process. arXiv preprint arXiv:170509718. 2017;.

[2] Murray PJ, Maini PK, Baker RE. The clock and wavefront model revisited. Journal of theoretical biology. 2011;283(1):227–238.

[3] Murray PJ, Maini PK, Baker RE. Modelling Delta-Notch perturbations during zebrafish somitogenesis. Developmental biology. 2013;373(2):407–421.

[4] Morelli LG, Ares S, Herrgen L, Schröter C, Jülicher F, Oates AC. Delayed coupling theory of vertebrate segmentation. HFSP journal. 2009;3(1):55–66.

[5] Wiedermann G, Bone RA, Silva JC, Bjorklund M, Murray PJ, Dale JK. A balance of positive and negative regulators determines the pace of the segmentation clock. eLife. 2015;4:e05842.